An experimental investigation of the passive control of reverse delta wing vortex flow structure and aerodynamics characteristics

Hongzhi Mou

Master of Engineering

Department of Mechanical Engineering

McGill University
Montreal, Quebec
December 2015

A thesis submitted to McGill University in partial fulfillment of the requirement for the degree of Master in Engineering
© Hongzhi Mou 2015

Abstract

This thesis summarises an experimental study of a 65-sweep reverse delta wing (RDW) by using a seven-hole pressure probe and a two-component force balance at Re = 270,000. Dye water flow visualization was also conducted in order to better understand the flow structure. Particular emphasis was placed on the variation of vortex flow quantities and critical flow parameters such as the core circulation, total circulation, tangential velocity and axial core velocity with change in chordwise locations from x/c = 0.2 to x/c = 1.5 for $\alpha = 10^o - 22^o$. Based on lift measurements, the RDW generated less lift from $\alpha = 8^o$ to $\alpha = 35^o$ in comparison with the conventional delta wing (DW). Hence, lift augmentation was attempted by attaching passive control devices such as a side edge strip (SES) and a leading edge strip (LES), made from aluminum strips with different widths, which were placed perpendicularly to the wing's bottom surface.

The flow field scans showed that the vortex flow underwent diffusion while it progressed in the chordwise direction. The size of the separated flow region, which originated from the spanwise vortex breakdown, increased with the angle of attack. Compared to a baseline RDW, RDW with SES generated a pair of more concentrated vortices with a higher core and total circulation values. Compared to a baseline RDW, the lift coefficient generated by the RDW with a 1.5% c SES and a 3% c SES increased by 0.18 to 0.28 on average, for angles of attack ranging from 0° to 40°. In addition, 1.5% c and 3% c SES boosted the wing's lift-to-drag ratio, for an average of 24% and 5%, respectively, from angles of attack of 10° to 20°. The dye flow visualization showed that the vortex flow generated by the RDW was located outside of the wing's surface and the vortex generated by the DW is located above the wing surface, in which suggesting the vortex lift is not applicable to a RDW.

ABRÉGÉ

Cette thèse résume une étude expérimentale sur les ailes delta inverses (ADI) à l'aide d'une sonde de pression de sept trous et d'une balance à deux axes à un nombre de Reynolds de 270 000. Visualisation à l'aide de colorant dans l'eau a été menée pour mieux comprendre les structures d'écoulement. Une emphase particulière a été portée sur la variation des quantités d'écoulement de tourbillon et des paramètres d'écoulement critiques tel que la circulation de base, la circulation totale, la vitesse tangentielle et la vitesse de base axiale en changeant l'emplacement en fonction de corde de $x/c = 0.2$ à $x/c = 1.5$ pour $\alpha = 10°$ - 22°. Selon les mesures de portance, les ADI génèrent moins de portance de $\alpha = 8°$ à $\alpha = 35°$ en comparaison avec les ailes delta (AD) conventionnelles. Par conséquent, l'augmentation de portance a été tentée avec les appareils passifs tel que des bandes de bord latéraux (BBL) et un bande de bord d'attaque (BBA), fabriqués à partir de bande d'aluminium avec différentes largeurs, lequel a été placé perpendiculairement à la surface du fond de l'aile.

Les champs de vitesse révèlent que le tourbillon a été diffusé pendant qu'il progresse dans la direction de la corde. La taille des régions des champs séparés, lequel qui est d'origine de la rupture du tourbillon d'envergure, augmente avec l'angle d'attaque. Comparé à la ADI non modifiée, les ADI avec BBL génèrent une paire de tourbillon plus concentrée avec une valeur plus haute de circulation de base et totale. Comparé à la ADI, le coefficient de portance généré par le ADI avec un BBL de 1.5%c et un BBL de 3%c augmente en moyenne de 0.18 à 0.28, pour les angles d'attaque de 0° à 40°. De plus, les BBL de 1.5%c et 3%c augmentent la finesse de l'aile, en moyenne de 24% et 5%, respectivement, des angles d'attaque de 10° à 20°. Visualisation avec colorant dans l'eau révèle que le tourbillon généré par la ADI été situé en

3

dehors de la surface de l'aile et le tourbillon généré par le AD est situé sur la surface de l'aile, ce qui suggère que la portance tourbillonnaire n'est pas applicable aux ADI.

Table of Contents

List of Figures

7

Nomenclature

α	Angle of attack
c	Wing chord
C_D	Drag coefficient $D/\frac{1}{2}\rho U^2 S$

9

C_L	Lift coefficient $L/\frac{1}{2}\rho U^2 S$
D	Drag
DW	Delta wing
$\mathbf{\Gamma}$	Circulation
L	Lift force
LEV	Leading-edge vortex
LES	Leading edge strip
r	Core radius
RDW	Reverse delta wing
Re	Reynolds number
VBD	Vortex breakdown
S	Wing projected area
SES	Side edge strip
SV	Spanwise vortex
u	velocity
U	Freestream velocity
ζ	Vorticity

Subscript

c	Core region
o	Outer region, Total
max	Maximum value
peak	Peak value

1. Introduction

The study of the reverse delta wing (RDW) is an interesting topic for researchers around the world. The most recent reverse delta wing study carried out by Altaf et al. [3] in which they have investigated the flow structure and aerodynamic characteristics of a 75 degree sweeping angle RDW at Re = 385,000. The research results were directly compared to a conventional delta wing (DW). The force balance results showed that the DW can generate more lift in comparison to a RDW at medium to high angle of attack. However, this high lift generation is associated with a high drag generation due to the vortex breakdown introduces low-axial-speed turbulent flow over the wing surface. Therefore, the lift-to-drag ratio of the DW is lower than the RDW at the same incidence when carrying out a comparison [3].

Due to the RDW aerodynamic performance superiority over the DW, the aircraft with the RDW configuration can potentially generate less drag than the aircraft with DW configuration at the take-off and landing stage. Consequently, less powerful engines are needed. Hence, this generates a lower fuel consumption requirement as well as a lower noise production. Furthermore, in the current study, a few passive control devices are attempted to overcome the shortage lift generation of the RDW. The methods of enhancing the lift generated by the RDW are inspired by the application of DW passive control devices, such as Gurney flaps and leading edge strips.

2. Background

Researchers around the globe have made efforts to use passive control devices to modify the aerodynamic performance generated by a delta wing. Devices such as leading edge flaps (LEF) and Gurney flaps (GF) can delay a delta wing's stall and boost the delta wing's performance respectively. The idea of a RDW aerodynamic performance augmentation is also inspired by the devices mentioned previously. In order to continue with the research of a RDW, a review of the aerodynamics of a conventional delta wing (DW) is carried out. Moreover, the application of leading ledge flaps (LEF), leading edge fences and GF of delta wing are reviewed. The current research of the RDW is summarized at the end of this chapter.

2.1. Delta wing aerodynamics

Research in the area of the reverse delta wing at low Reynolds numbers has not been carried out by many researchers yet. In order to compare the aerodynamic differences between a RDW and a conventional delta wing (DW), it's worth it to discuss the aerodynamic characteristics and flow structure generated by a DW.

Wind tunnel experiments demonstrate the flow differences at the sharp leading edge for a slender delta wing (sweeping angle > 55 degree) when it is positioned at a medium angle of attack. The flow separation at the sharp leading edge is called the separated shear layer of the vortex or vortex sheet [4]. The vortex sheets roll up and form two counter-rotating vortices located above the delta wing surface in the vicinity of the leading edges in the spanwise direction (see Figure 1(b)). The two counter rotating vortices located above the delta wing surface are called the leading edge vortices, or LEVs. The schematic diagram for the shear layers and the LEV structure is illustrated in Figure 1 [5]. As illustrated in Figure 1(a), the tangential velocity,

12

which is shown in the plot over the vortex on the left, is developed across the vortex core and is asymmetric. The vortex core is jet-like, due to the low pressure gradient developed inside of the core. Schematic diagram of the axial velocity is shown in the plot over the right vortex. The diagram is only true for measurements taken upstream of the vortex breakdown, which will be explained later in this section [2, 4]. The formation of the jet-like core is due to the vortex sheet spiraling around the vortex while the vortex evolves downstream. The spiraling of the vortex is in the same direction as the vortex axis, resulting in an core axial flow acceleration [5]. The formation of the jet-like core results in very low pressure developed in the vortex core region.

As illustrated in Figure 1 (b), a secondary vortex is formed over the wing's surface, which is located closer to the wing's top surface when compared to a LEV. The secondary vortex is formed and moving in the opposite direction of the LEV. Unlike the LEV, the secondary vortex is always wake-like [1, 6-8].

A more in-depth investigation of the delta wing LEV was provided by Earnshaw [1]. Based on Earnshaw's study, the LEV has been divided into three regions: the shear layer, which is the roll up sheet of the vortex, the rotational core and the viscous sub core. A schematic diagram is provided in Figure 2. As illustrated in Figure 2, some small size eddies have been fed into the vortex. This observation suggests that the formation of the shear layer has a structure similar to Kelvin–Helmholtz instabilities. This shear layer increases its size or thickness as the vortex evolves downstream. Based on Earnshaw's observation, the diameter of the rotational core and the viscous sub core are respectively 30% and 5% of the local semi-span. The 5% local semi-span diameter contains both high axial velocity gradients and high static pressure gradients.

The very low pressure developed inside of the vortex core is also the mechanism responsible for the additional non-linear lift generation over the wing's top surface. The additional lift superimposed onto the delta wing's surface is also called the vortex lift, or the non-linear lift [4]. At low and moderate angles of attack, the contribution of the vortex lift is proportional to the sweeping angle [2] at particular angles of attack.

As the angle of attack increases, the static pressure inside of the vortex core region continually decreases and in turn, the core axial velocities continue to increase. The vortex lift is consequently increased due to the drop in core static pressure [9], as shown in Figure 5. The lift prediction, through the usage of the Kutta-Joukowski theorem has been done by Kaplan in 2007 [10].

2.1.1 Vortex breakdown

As the angle of attack continues to increase, a sudden expansion of the vortex core occurs near the trailing edge of the wing. This sudden expansion of the vortex core is always associated with an abrupt drop in the core axial velocity as well as a massive decrease in the core maximum tangential velocity [11]. This phenomenon is known as the vortex breakdown (VBD) or vortex bursting. Experimental observation shows that a strong turbulence is introduced to the flow field downstream of the VBD point [11]. In turn, the VBD location will progress upstream as the angle of attack increases. If the angle of attack is high enough, the VBD will reach the apex of the wing [12].

Many researchers [13-15] have studied the VBD and it has been observed that due to the unsteady nature of the flow introduced to the flow field, the unsteadiness of the flow field may affect the delta wing aircraft stability and the VBD may cause wing buffeting [16].

14

Due to the unsteady nature of the flow introduced by the VBD, the downstream flow of the VBD point is distorted and disorganized. The delta wing's top surface will experience a substantial change in the local pressure field downstream of the VBD point. Consequentially, the disorganization of the vortex will bring detrimental effects to the vortex lift generation over the delta wing surface as well as a boost in drag production [11]. Hence, with the existence of the VBD over the delta wing's surface, the lift curve slope is decreased and the pitch-up moment is increased [12]. The VBD location is very sensitive to the delta wing sweeping angle and angle of attack [4, 12].

Since the delta wing's VBD location is a sensitive function of the wing sweeping angle, several control devices such as variable sweep [4, 17-20], small apex flap [12, 21], oscillating leading edge flaps [16] and leading edge blowing [5] have been applied to control the VBD location to boost the wing performance or control the wing buffeting.

2.2. Passive control devices for the delta wing

This section discusses several passive control devices and their effects on a conventional delta wing aerodynamic performance as well as the LEV flow structure. The basic passive control devices are: leading edge flaps (LEF), leading edge vortex flaps (LEVF), leading edge fences and Gurney flaps (GF). LEF and LEVF are used to modify the LEV structure and therefore manipulate the vortex lift generation of a DW. GF is used to enhance lift with a moderate increase in drag. Therefore, enhancing the delta wing aerodynamic performance. Leading edge fences, on the other hand, are used to increase the lift at low speed; it is therefore beneficial for aircrafts with delta wing configuration at the landing stage. There are some complicated devices for delta wings, such as: wing dihedral and anhedral, oscillating leading

edge flaps, leading edge with streamwise blowing and variable sweep. The effects on the delta

wing aerodynamics performance and LEV structures provided by these devices are well

documented [22-24]. This section will discuss the functionality of the aforementioned basic

passive control devices.

Table 1, Summary of the delta wing control devices

Reference	Λ	α	c	Re × 10^3	Instrumentation	Control device	Oscillation or static
L.W. Traub and S.F. Galls [7]	70	20^2	400 mm	80^1 1120^2	Smoke wire and Kiel probe	LEF and GF(0.5%c and 0.95%c)	Static
C.-H. Kuo and C. W. Hsu [25]	60	25^2	200 mm	$15^{1,2}$	Fluorescent dye and LDA	LEF (5 degree flap angle)	Both
K. Rinoie [26]	60	$-4\ to\ 36^2$	1.15m	2000^2	Surface pressure measurements	leading edge vortex flap (LEVF) and rounded edge	Static
S.Oh and D. Tavella [27]	N/A	N/A	N/A	N/A	Theoretical method	LEVF deflected downward	Static
J.F.Marchman III [28]	60 75	0 to 45	31.6'' and 45.7''	2000^2	Force balance	LEF and tapered LEF	Static
Q. Deng and I. Gursul [16]	70	20, 25	254mm	50^2	LDV	Oscillating leading edge fences	Oscillation
C.S.Rdeey [29]	74	5 and 20	N/A	N/A	Simulation	Leading edge fences upward	Static
D.I. Greenwell [30]	40 60 70	-15-30	246,353 and 436mm	700^2	Force balance	Gurney flaps (1,3,and 6% c)	Static
M.D. Buchholz and J.Tso [31]	60	-5-20	635, 439.7 and 609.6 mm	860^2	Force balance, flow visualization and pressure measurements	Gurney flaps	Static
JX. Zhang and JJ.Wang [21]	70	20-50	250mm	316^2	Force Balance	Drooping apex and Gurney flaps	Static

---

[1] Reynolds number used for flow visualization
[2] Reynolds number used for flow field survey and/or force balance tests etc.

17

2.2.1. Static leading edge flap (LEF) and leading edge vortex flaps (LEVF) deflected downward

Leading edge flap (LEF) is a small piece of strip bent perpendicularly to the wing's top surface. The strips are attached to the wing's leading edge, as illustrated in Figure 2. The strip's size is constant throughout its chordwise directions. On the other hand, the leading edge vortex flap (LEVF) is a device which is made by bending a portion of the wing to a certain deflection angle (see Figure 7). The bending point of the device starts from the apex of the DW and ends at a location on the wing's trailing edge. Therefore, the local heights of LEVF are proportional to the wing's local semi-span or local span. The main function of the LEF is to modify the leading edge flow separation and therefore modify the LEV flow structure to create a delay in VBD as well as a drag reduction at medium and high angles of attack [7]. The purpose of the LEVF is to concentrate the suction of the LEV on the flap. Therefore, the vortex-induced loading on the flap can provide thrust and in turn oppose the drag when it is deflected downward [32]. Both the LEF and the LEVF can improve the DW aerodynamic performance at medium to high angles of attack [33, 34]. This sub-section will summarize the experimental investigations of the effect of downward bended LEF and LEVF, attached to the bottom surface of the wing. A numerical modeling of the LEVF is also summarized at the end of this sub-section.

An investigation of downward deflected LEF effects was provided by Traub et al. [7].The study was done by using a force balance and a Kiel Probe. A DW model with a 70 degree sweeping angle full delta wing was utilized (as illustrated in Figure 2). The LEF heights ranged between 0.5% and 0.95% chord of the wing.

18

The force balance data acquired for the study shows that the LEF has no effect on C_L until high incidence occurs. The wing with the leading edge flap increases the $C_{L_{max}}$ by 6% over the baseline delta wing. Moreover, the leading edge flap shows that the LEF can either have an equivalent or better aerodynamic performance of the baseline wing over the range of the angle of attack.

The flow visualization reveals that the LEF can delay the trailing edge onset the VBD angle by approximately 2 degrees. This reduction in initial onset VBD angle may be due to the flap imparting a positive leading edge camber to the wing. Due to the presence of the camber, the LEV is weakened, hence delaying breakdown.

A Keil probe is used to investigate the flow field over the delta wing surface at a location of x/c = 0.7 and at a 20 degree angle of attack. The results of the investigations demonstrated that the LEF has the ability to reduce the thickness and the strength of the primary vortex shear layer. This is due to the LEF trapping the fluid particles underneath the wing, leading to a reduction in the interaction between the shear layer and the secondary vortex.

An investigation of downward deflected LEVF effects was provided by Kuo et al. [25] The latter applied a leading edge vortex flap to a 60 degree sweep angle half delta wing (as illustrated in Figure 4). The investigation was carried out at a 25 degree angle of attack with different static flap deflection angles. The experiment was using LDA flow field surveys and dye flow visualization. The main purpose of the study is to achieve vortex breakdown delay.

The dye flow visualization confirmed that a secondary vortex is generated over the LEVF when there is no flap deflection angle. In turn, the behaviour of the vortex resembles that of a vortex generated by a baseline delta wing. When a small flap deflection is applied (i.e. 10

19

degree), a small vortex core can be identified over the LEVF. However, no vortex is formed over the wing's body surface with such a small flap deflection. The primary vortex core moves inboard and is located over the hinge line as the deflection angle increases to an angle of 10 degree. As the flap deflection angle increases, the size of the LEV increases significantly and shifts further inboard and locates over the DW. Moreover, two small vortices can be found near the hinge line.

The flow visualization results indicated that for a small flap used in this study, a vortex is located over the flap at a small flap deflection angle (i.e. 10 degree). The location and the size of the vortex suggest a small amount of thrust is developed in order to oppose the drag. However, the flap vortex moves inboard and is eventually located above the wing's surface as the deflection angle increases.

A more in depth experimental investigation pertaining to the effects of the LEVF was provided by Rinoie [26] using a force balance device and several surface pressure taps. His study used a 1.15 meter chord and a 60 degree sweep DW with LEVF at different deflection angles (as illustrated in Figure 7). As summarized earlier, the main purpose of the LEVF is to provide thrust by producing a vortex over the flap and to also oppose the drag. In this study, the formation of the flap vortex is also manipulated by modifying the sharp leading edge profile to a round shape with different rounded radius. The purpose of the modifications of the DW was to minimize the drag generated over the delta wing. Also, force balance results were carried out in order to compare the effects of the LEVF and to round the radius of the leading edge to the DW performance.

20

The results indicated that the increase in the radius of the rounded leading edge reduces the drag regardless of the LEVF deflection angle. The size (spanwise length) of the suction pressure region on the flap is also reduced with an increasing rounded leading edge radius.

The DW with a rounded leading edge profile can provide a drag reduction to the wing and a 10% improvement in lift-to-drag ratio for a $C_L > 0.2$ is observed compared to the DW with a sharp leading edge. In addition, deflecting the rounded LEVF improves the L/D ratio at $C_L > 0.5$. A 25% increase in the L/D ratio is observed for a 30 degree LEVF deflection, with a 30mm diameter rounded leading edge profile, when compared to the wing with a sharp edged LEVF for a C_L between 0.6 and 0.8.

A numerical investigation of the delta wing LEVF was provided by Oh and Tavella [27]. The numerical solution is prepared using vortex-feeding-sheets singularity systems in order to represent the separated flow (as illustrated in Figure 6). The objective of the study is to numerically predict the lift and drag generated by the DW with the LEVF.

In this study, two distinct vortex singularities are used to represent the LEVF vortex over the flap and the vortex generated over the wing body. In order to relieve these singularities, two Kutta conditions are invoked. Pressure integration is used to calculate the lift and drag forces on the wing components. The equation for the L/D indicates that for a given flap deflection angle, a propulsive component force is developed over the flap. Hence, a decrease in the DW drag could boost the L/D ratio.

2.2.2. Leading-edge fences, LEF and LEVF deflected upward

The previous sub-section summarizes the effect of downward deflected LEF to a DW. In some cases, the LEF was deflected upward the wing surface. Therefore, a different vortex flow

21

was developed by these upward deflected flaps. As mentioned previously, the heights of the LEF are constant throughout its chordwise direction. The leading edge fence, on the other hand, is a strip that is always deflected upwards. The leading edge fence resembles a LEVF that has only been deflected upward; the height of the fence is proportional to the DW local span or semi-span. Hence, the fences are constantly in a triangular shape with an induced angle (i.e. the strip is inclined). A stable vortex is trapped behind the fences or the LEF when it is deflected upward at low angles of attack. The purpose of the fences or the upward deflected flap attached to the delta wing is to develop more drag and lift for the DW aircraft and hence reduce the landing speed or the angle of attack.

Marchman et al. [28] used upward deflected LEFs and leading edge fences with a range of deflection angles for both 60 and 75 degree sweeping angle delta wings (as illustrated in Figure 8). The investigation was able to provide an understanding of the effect of these control devices in the DW aerodynamic performance. The lift curve generated by the 60 degree sweeping angle delta wing shifted to the left. The shift in question is similar to the way in which a camber effect would shift the curve (i.e. the zero lift angle of attack is shifted to negative). The $C_{L_{max}}$ is reduced by 16%. It is suggested that a stronger vortex is formed at a lower angle of attack compared to a BW DW. Therefore, a stronger vortex lift occurred at lower angles of attack compared to the BW DW. A 70% lift increase is observed for 5 degree angle of attack. This fulfills the purpose of the upward deflected LEF, which is to create a vortex lift at lower angles of attack where it would not normally exist. However, due to the mechanism of the LEF, a 10 degree decrease in stall angle is also observed.

Associated with the lift increase at low angles of attack, the drag is also increased at this range. This suggests a suction force provided by the vortex trapped behind the flap moving in the

22

same direction as the drag. Due to the drag increase, a large drop in performance at low-to-medium angles of attack is observed. The increase in drag generated at low angles of attack is still beneficial for aircrafts with delta wing configurations, especially for the aircrafts in the landing stage. A high lift generated by the LEF would allow a lower speed approach at lower angles of attack and the high drag generated by the LEF would serve the purpose of slowing the aircraft down.

The test on the 75 degree sweep delta wing is similar: with the presence of the upward deflected LEF, the lift coefficient is increased up to 100% at a low angle of attack and a 14% decrease in $C_{L_{max}}$ is observed. The drag does not increase as significantly as the one for the 60-degree delta wing. For the tapered flap (leading edge fence with induced angle), compared to a flap with a constant chord size, the increase in the lift coefficient is almost identical at low range of angle of attack. However, only a 2% reduction in the maximum lift coefficient is observed. The lift generated by the wing with leading edge fences is almost identical to the one generated by a BW.

Different flap deflection angles are tested on the 60 degree sweeping delta wing as well. It is observed that both C_L and C_D increased while the lift-to-drag ratio decreased as the flap deflection angle increased. A minimum reduction in the $C_{L_{max}}$ is observed for wings with a 10 and 20 degree LEF deflection angle.

It is observed that a decrease in the flap size is associated with a decrease in lift and drag at LEF deflection angle of 20. The decrease in the drag overshoots the decrease in the lift, therefore an L/D increase is observed.

The hypothesis made earlier stating that the flap vortex can provide a suction force to generate drag was confirmed by Buchholz et al. [31] by using pressure tabs. They used a 60 degree sweep delta wing with leading edge fences at different induced angles (as illustrated in Figure 9). Flow visualization was conducted to understand the vortical flow trajectory. Pressure taps are located on the surface of the wing as well as the flaps at several chordwise locations to provide surface measurements. The force balance results demonstrated that the delta wing produced a higher lift with a greater fence induced angle at low angle of attack. The gain in lift is higher below the 5 degree angle of attack compared to the gain in lift at a higher incidence (> 5 degree). Drag is also increased at the highest level below the 5 degree angle of attack and remained nearly unchanged at higher angles of attack. The L/D ratio was carried out against the lift coefficient. The plot suggests that the L/D ratio decreases as the leading edge fence induced angle increases.

Flow visualization showed that a pair of vortices can be seen at a 6 degree angle of attack and the vortex bursting is around 14 degrees over the aft portion of the baseline DW. The pair of vortices can still be observed for the DW with a 5 degree leading edge fence induced angle at a 6 degree angle of attack. However, this pair of vortices has a strong transient VBD behaviour. As the angle of attack increases to 10 degrees, the bursting point moves above the wing and stays at a relative steady location. Compared to the baseline DW, the presence of leading edge fences can cause the VBD to reach the trailing edge of the wing prematurely.

Surface pressure investigation is also carried out. The results showed that for baseline DW, the suction pressure is the highest at the location near the apex and gradually decreases as increases occur in chordwise direction. Generally, the suction pressure increases its magnitude as the angle of attack increases. The peak location of the suction pressure is the consequence of the

24

LEV's position over the wing. The surface pressure measurements confirmed that the primary vortex imposed a strong suction to the surface of the wing and fences at a 0 degree incidence. The suction provided by the vortex will disappear at a location aft of the wing with increasing angles of attack due to premature VBD.

Both the surface pressure distribution and the flow visualization indicated that the increase in lift and drag is the result of trapping the vortex behind the fences at low angles of attack (angle of attack < 5). Cross-stream suction is observed due to the trapping of the vortex. Effective thickness and camber is added to the wing and in turn increased the lift [35, 36]. However, the fence will deteriorate the lift at a higher incidence due to premature VBD.

2.2.3. Gurney flaps on delta wing

The Gurney flap (GF) is a sample device made from a short flat plate usually bent perpendicularly to the chord of an airfoil. The GF is often attached to the trailing edge of an airfoil. It was invented by the racing car driver and team owner Daniel Gurney [37] in the 1960s. The downforce generated by the car while cornering is enhanced with a GF attached on the spoiler pressure surface. The augmentation of the downforce is associated with a minimum penalty of drag. At low Reynolds numbers, experimental investigations and CFD simulation results are well documented for a GF [38-42] mounted on the bottom surface of an airfoil. Other than the effect of a GF on an airfoil, the Gurney flap can also increase the maximum lift coefficient and reduce the zero-lift angle of attack of a DW. Many researchers have given a lot of attention to the research pertaining to the GF effect on delta wings.

Buchholz et al. [31] showed that the lift coefficient increases with an increasing GF size. A decrease in the lift curve slope is observed at around a 10 degree angle of attack. Moreover,

the gurney flap leads to an initial vortex breakdown at lower angles of attack when compared to the BW DW. The results suggest the gurney flap produced a higher pressure on the lower wing surface, therefore causing more flow to circulate around the leading edges, in turn increasing the swirl angle and leading to earlier breakdown. The force balance results showed that at a high lift coefficient, the lift to drag ratio is higher than the BW DW.

Traub et al. [7] also showed that the delta wing lift coefficient increased with a gurney flap attached at all angles of attack. The zero-lift angle of attack shifted to negative and no changes in the lift's curve slope occurred. The lift's curve slope suggests the flap primarily affects the potential flow of the lift component. The results indicated that the lift increment caused by the gurney flap is growing with increasing flap height. The drag polar indicated that the gurney flap is seen to reduce the drag at a moderate to high lift coefficient. Furthermore, the lift-to-drag ratio is improved by the presence Gurney flap for a medium lift coefficient. However, a reduction in the peak lift to drag ratio is observed.

Wang et al. [21, 36] also studied the effects of gurney flaps on a 70 degree sweeping angle delta wing (as illustrated in Figure 10) by using a force balance. The experimental results showed that the Gurney flap provided a boost in lift at low angles of attack (< 25 degree). It is suggested that the Gurney flap, at the trailing edge of the wing, changes the Kutta condition when compared to the delta wing without the gurney flap. Also, the force balance results indicate that the gurney flap, with all the flaps tested in this study, will decrease the wing's stalling angle with an increase to the maximum lift coefficient of the DW. The gurney flap shifted the curve upward and slightly to the negative angle of attack direction. It is suggested that the gurney flap served to increase the effective camber of the wing.

2.3. Current research into the reverse delta wing

A review of the research of RDW is provided in this section. As described in the earlier section, many researchers have paid close attention to the DW and its control. In comparison, only a few researchers have investigated the aerodynamic performance and the flow structure of a RDW, perhaps because the RDW cannot generate as much lift as the DW. However, Altaf et al. [3] have found that despite the fact that the RDW generates much less lift than the DW, less drag is generated by the RDW compared to the drag generated by the DW from medium to high angles of attack. Therefore, the RDW has a better aerodynamic performance than a DW. Therefore, it is interesting to investigate the RDW flow structure and aerodynamic performance. This section summarizes the current research into the RDW in general and a review regarding the application of a reverse half delta wing (RHDW) is also carried out.

Table 2, Summary of the research of a RDW (or RHDW)

Reference	Λ	α	C	Re $\times$ 10^3	Instrumentation	Control device	Oscillation or static
A.Altaf et al. [3]	75	5-20	488mm	382^2	PIV, force balance and simulation	N/A	Static
T.Lee and Y.Y. Su [43]	65	$10, 25^1$ $4 - 12^2$	280mm	30^1 245^2	Smoke wire, flow vis., Force balance and SHP	RHDW	Static

[1] Reynolds number used for flow visualization
[2] Reynolds number used for flow field survey and/or force balance tests etc.

2.3.1. Study of the full reverse delta wing (RDW)

Force balance results were carried out using a six-component force balance at Re = 382,000 [3]. The RDW used in the study was a 74.49 degree sweeping angle reverse delta wing with a bevel angle of 20 degrees. The lift and drag coefficient is compared with a DW with the

same sweeping angle. The results indicated that the RDW generated a lower C_L and C_D than a DW at all angle of attack tested. However, a higher L/D ratio is observed for the RDW when compared to a DW due to the reduction in drag from low to medium angles of attack.

Flow field survey results showed that the RDW vortex had a non-axis-symmetric shape at x/c = 1.359. This indicates the fact that the vortex had not been fully developed. Further down of the wing (x/c = 3.418), the velocity vectors showed the vortex had an axisymmetric shape. The velocity vector field showed that at locations x/c = 1.359 and x/c = 3.418, the DW vortices have doubled in tangential velocity magnitudes compared to the RDW at a 20 degree angle of attack. Indicating vortex rotation speed is higher.

The tangential velocity is increased for both the RDW and DW vortices as the angle of attack increased. However, at the same angle of attack, tangential velocity is decreasing as the chordwise distance increases for both the RDW and the DW. It suggest that the decrease in tangential velocity may be due to viscous dissipation.

CFD simulation results are also carried out (Figure 11). The streamline contours indicated that the RDW tip vortex is located outside of the wing's surface. Also the RDW tip vortex originates from the spanwise vortex developed in the vicinity of the leading edge of the wing. The CFD simulated pressure distribution over the DW's bottom surface has a higher average magnitude than the pressure distribution generated on the lower surface of the RDW. Over the top surface of the DW, a streak of low static pressure field is observed close to the DW leading edge. This suggests that the vortex over the top surface provides vortex lift to the wing. This is also suggested by the CFD streamline contours. The average pressure on the top wing

28

surface generated by the DW is much smaller than the average pressure generated by the RDW [3].

2.3.2 Flow control by using half reverse delta wing (RHDW)

The aforementioned difference in static pressure resulted in the fact that the DW generated a much higher lift than the RDW. Lee and Su [43] used a RHDW attached to a NACA 0012 wing to control the induced drag generated by the wing at Re = 245,000. In order to understand the effect of the RHDW, smoke wire flow visualization is carried out at Re = 30,000 for a full RDW. The results demonstrated that the two tip vortices generated by the full RDW lie outside and above the wing when a smoke wire is positioned below the wing surface. When the smoke wire is positioned above the wing surface, the separated flow region located above the wing is clearly observed. The results suggest that the separated flow region is triggered by the spanwise vortex breakdown. The tip vortex generated by the full RDW becomes further diffused as the angle of attack increases. The flow field survey and force balance measurements were carried out at Re = 245,000. The flow field survey is carried out using a seven-hole pressure probe. The results demonstrated that the RHDW has modified the formation of the tip vortex. The modification resulted in a lift-induced drag reduction compared to NACA 0012 with squared tip.

2.4. Objective

The background describes the methods to increase the lift-to-drag ratio of a DW by using methods to modify the DW leading edge shape, consequently, manipulating the formation of the LEV, VBD location and the suction forces provided by the LEV. The GF was also used on the DW to provide a better potential lift generation compared to a baseline DW. A summary of the

current study into the RDW is provided in the background section with flow field survey downstream of the wing. However, the detailed flow field survey around the RDW is still needed. The objective of the research is to carry out a detailed flow structure study of a 65 degree sweeping angle RDW using a seven-hole pressure probe at different streamwise locations and angles of attack ($10^o - 22^o$). The flow field survey for both DW and RDW are also carried out at selected angles of attack. Dye flow visualization will also be conducted for a better understanding of the RDW vortical flow structure. A two-component force balance is applied to measure lift and drag. In addition to the investigation of a baseline RDW, the flow structure of a RDW with passive control devices such as side edge strips (SES) and leading edge strips (LES) will also be investigated at selected angles of attack.

3. Experimental Method and Apparatus

3.1. Wing model

The wing model used in this study was a reverse delta wing with 65 degree sweeping angle and 15 degree beveled sharp edges, as illustrated in Figure 12. The wing had a chord length of 41.91 cm and a span of 40.88 cm. The model was machined from a flat aluminum plate with a thickness of 0.65 cm (1.5% c).

A baseline regular delta wing model with the same dimensions was also used. This model was used to compare its leading edge vortex structure to the vortex structure generated by reverse delta wing. Figure 12 shows the details of the wing model.

The passive control devices used in this study are side edge side strips and leading-edge strips. They were fixed to the wing's top and bottom surfaces using double sided tape. Two sets of side edge strips with different heights were used.

The heights of strips were 1.27 cm (3% c) and 0.635 cm (1.5% c) respectively. Both sets of strips were bent from 0.3175 cm thick 2.54 cm wide aluminum plates. All the strips were bent to 75 degrees between the sticking surface and the windward surface, resulting in the strips' windward surfaces to be perpendicular to the wing's suction surface. All the strips were bent at the middle of its width and sheared to a length that covers the entire length of the edge of the wing. The strips' longitudinal edges were made sharp and the strip did not have a bevel.

For flow field measurements, the wing model was secured by three 10-24 flathead screws horizontally on a vertical support, as illustrated in Figure 13, mounted on a 1.905 cm thick plate fixed to the tunnel floor. The cross-section of the vertical support was CNC machined to be the

31

shape of a NACA 0012 wing to minimize the disturbance created by the support. The origin of the Cartesian coordinate system was measured from the center of the leading edge of the wing at 0 degree incidence, with x, y and z aligned with the streamwise, vertical and horizontal directions, respectively.

3.2. Flow facility

All the experimental work was conducted in the J.A. Bombardier low-speed suction type wind tunnel, as illustrated in Figure 14, located in Aerodynamics Laboratory of McGill University. This open-loop wind tunnel has a contraction ratio of approximately 10:1. 10 mm honeycomb flow straighteners are placed at the inlet of the wind tunnel with 4 screens behind the honeycomb for flow conditioning. A 3-meter long contraction section is located downstream of the screens. The test section freestream turbulence intensity is less than 0.05% at 35m/s.

The test section is rectangular, and its dimensions are: 0.9 meter by 1.2 meter by 2.7 meter in vertical (y), horizontal (z) and streamwise (x) direction. The test section is followed by a 9-meter long diffusor section. A 16-blade, 2.5m diameter vibration isolated fan is located aft of the diffusor section. The fan is powered by a variable-speed AC motor equipped with an acoustic silencer. A miniature Pitot tube is used to determine the tunnel flow speed. This Pitot tube is connected to a Honeywell DRAL 501-DN differential pressure transducer with a maximum water head of 50 mm. The transducer resolution is 97 Pascal/Volt and its response was linear to within 1%

3.3. Traversing mechanism

A two degree of freedom traverse was used to move the seven-hole pressure probe (SHP) (as illustrated in Figure 15). The probe is aligned horizontally on the arm of the traverse. The y-direction traverse and z-direction traverse were powered by Sanyo-Denki model 103-718-0140 stepper motor and Bio-dine model 2013MK2031 stepper motor respectively. A NI PCI-7344 4-axis motion controller, which was controlled through LabVIEW, was used to control the traversing. Automated scanning was provided by synchronising the controller with the data acquisition system. The positioning accuracy of the traverse was determined to be within 20 μm and 60 μm for y and z direction respectively. The total test section blockage due to the traverse was estimated to be 8%.

3.4. Two-component force balance

For force balance measurements the test model was mounted vertically by using an arm made from thin aluminum plate with a thickness of 0.635 cm (as illustrated Figure 16 and Figure 17). The force balance arm was chamfered to minimize disturbances generated by the arm. The arm was secured on top of a cylinder rod by using 10-24 standard screws. The cylinder support was mounted directly on the sensor plate of the force balance. All lift and drag force measurements were obtained from an external two-component force balance located below the wind tunnel. The force balance was mounted on a turntable that was installed in the test section floor. Two sets of flexures were used to support the sensor plate, y direction flexures and z direction flexures. The y direction is parallel to the wing chord and the z direction is normal to the wing chord. Each cantilever-type spring flexure had a maximum deflection of 4mm.

Two Sanborn 7DCDT-1000 linear variable differential transformers (LVDT) were used to measure flexure deflections independently. Both LVDT responses were linear to within 1% in the calibration range used. The force balance was calibrated in situ over a range of force increments and the resolution of the LVDTs was 0.0931 N /mV in the y direction and 0.0481N /mV in the z direction.

3.5. Seven-hole pressure probe

The probe tip was made from brass and machined to a 30 degree cone angle. The tip of the probe had a diameter of 2.7 mm and seven 0.5 mm diameter holes drilled parallel to the sting axis, six of which were arranged on a 2.4 mm diameter circle (as illustrated in Figure 18). The probe had a 130 mm long shaft, and the shaft was fixed to a 12 mm diameter, 400 mm aluminum probe sting.

A set of 1.6 mm diameter, 550 mm long Tygon tubing was used to connected the pressure taps and the pressure transducer array box. The Tygon tubing was passed through the probe sting. The pressure transducer array box was fixed on the arm of the traverse and it contained seven Honeywell DC002NDR5 differential pressure transducers with a maximum head of 50 mm water. The reference pressure for all transducers was the ambient atmospheric pressure measured from inside a fibreglass covered damping unit. The output of the transducer array was connected to a custom-built signal conditioner. The signal conditioner consisted of a seven-channel analog signal differential amplifier with a gain of 5:1 and an external DC offset. The resolution of the pressure transducers was on average 61 Pascal/Volt and their response was linear to 2%. The probe was calibrated in-situ, using the calibration procedures described in Wenger and Devenport [44].

3.6. Data acquisition and reduction

A 16-channel, 16-bit NI-6259 A/D board was used to acquire data. This A/D board was powered by a Dell Dimension E100PC, which was used to collect and store data. A NI BNC-2110 connector box was used to connect A/D board and sensor output. Output voltages were sampled at 500Hz for 9 seconds (including a 2 seconds traverse mechanism motion settling time) in order to obtain reliable average for recording. Other sampling frequencies and longer sampling times were also tested to ensure convergence, but the differences were less than 0.1 mV. The reduction flow chart is shown in Figure 19.

All the fluctuations were damped out by the Tygon tubing between the pressure transducer and the SHP. Therefore, only time averaged mean voltage output has been recorded and processed. Flow field measurements were taken at a perpendicular to the free stream flow direction cross-stream plane, which is positioned at several chordwise locations from 0.2 to 1.5 x/c. The size and boundaries of the scan grid were varied to accommodate the growth and trajectory of the vortex. For example, the flow field measurements obtained using the grid shown in Figure 20, where higher resolution grids with smaller spacing ($\Delta z = \Delta y = 3.175 mm$) were applied to the area of vortex core and vortex arm. The coarse grids with large spacing ($\Delta z = \Delta y = 6.35\ mm$) were applied to the separated flow zone in order to save data recording time. A coarse grid will result in lowering scan resolution, and lowering the scan accuracy. Data recorded by using the lower resolution grids were linearly interpolated to the higher resolutions in order to minimize error.

Several quantities such as vorticity, circulation and tangential velocity were derived from the velocity data.A second-order difference scheme was used to calculate the axial component of vorticity, such that:

35

$$\zeta_{i,j} = -\left(\frac{\partial v}{\partial z} - \frac{\partial w}{\partial y}\right) \approx -\left(\frac{v_{j+1,i} - v_{j-1,i}}{2\Delta z} - \frac{v_{j,i+1} - v_{j,i-1}}{2\Delta y}\right)$$

Where $i = 1, 2, 3, \ldots, m$ and $j = 1, 2, 3, \ldots, n$ and m and n are the number of points in vertical and horizontal directions. A central difference was used on interior data pints, while forward and backward differences were used on points on the edges of the measurement grid.

The circulation was found using Stokes' theorem which can numerically integrating the product of vorticity and area. The core and outer circulation were calculated as follows:

$$\Gamma_c = \sum\sum \zeta_{i,j} \times \Delta y \Delta z \qquad r_{i,j} < r_c$$

$$\Gamma_o = \sum\sum \zeta_{i,j} \times \Delta y \Delta z \qquad r_{i,j} < r_o$$

Where:

$$r_{i,j} = \left(z_j - z_c\right)^2 + (y_i - y_c)^2$$

$$r_o = r\left(\Gamma = 0.95\Gamma_{max}\right)$$

The origin for the polar coordinates was set to the vortex center (z_c, y_c), the peak vorticity location, and the core radius, r_c as defined by the distance between the vortex center and where the maximum tangential velocity location.

The tangential velocity v_θ was also calculated from polar coordinates as follows:

$$v_{\theta_{i,j}} = \left(v_{i,j} - v_c\right)\sin\theta - \left(w_{i,j} - w_c\right)\cos\theta$$

Where θ is the polar angle relative to the vortex center.

4. Result and discussion

This chapter discusses the experimental results for the 65 degree reverse delta wing (RDW) with its aforementioned control devices, i.e. SES and LES, at Re = 270,000. Section 4.1 presents the force balance results obtained by the RDW with different passive control devices. Section 4.2 discusses the flow field differences between the RDW and the DW, based on flow field surveys by using the SHP at $\alpha = 18^o$ and chordwise locations from x/c = 0.3 to x/c = 1.5. A detailed discussion of the chordwise RDW vortex evolution at several chordwise locations at different angles of attack is carried out in Section 4.3. The mechanism triggering the vortex diffusion is also being discussed with the aid of dye flow visualization. Moreover, the differences in the vortex characteristics between the RDW baseline wing and the RDW with different passive control devices are investigated over the wing's chordwise locations in Section 4.4. The differences in vortex evolution with an increasing α between configurations is discussed in Section 4.5.

4.1. Aerodynamic performance

The results of the force balance measurements are discussed in this section. Based on the previous research by Altaf et al. [3], a RDW generates less lift than a DW. However, the aerodynamic characteristics of a RDW can be manipulated by the use of passive add-ons such as side edge strip (SES) and leading edge strips (LES). The goal of such manipulations is to increase the aerodynamics performance of a RDW. The results are also directly compared with the lift generated by a DW.

37

4.1.1 Lift coefficient

The lift coefficients generated by different wing configurations have been plotted in Figure 21. The results are directly compared with Altaf et al. [3] lift measurements using a 75 degree sweeping angle RDW at a Reynolds figure of 382,000. It can be observed that the conventional delta wing (DW) platform does produce higher lift than the RDW. Based on numerous researchers' work, as mentioned earlier in Chapter 2, the presence of the concentrated leading edge vortex (LEV) introduces vortex lift to the DW. This vortex lift is provided by the suction force generated by the proximity of the LEV to the wing's upper surface. The DW produces a sharper stall and the RDW stalls more gradually under the comparison. The stalling angles of both wings are about the same ($\alpha_{ss} = 34°$ and $\alpha_{ss} = 36°$ for the DW and RDW respectively). As compared to the DW, the RDW does not have a pair of stable LEV to provide suction forces over the wing's surface, as suggested by the CFD simulations carried out by Altaf et al. [3].

The RDW lift can be significantly boosted if the SES is utilized. Increasing further the strip height increases the lift. The lift increase can partially be explained by the SES rising the pressure on the bottom surface of the RDW. As illustrated in Figure 21, the zero-lift angle of attack shifts to negative with the presence of 1.5% c SES and 3% c SES. The zero-lift angle of attack has been shifted to the negative due to the SES introducing positive chordwise camber to the wing. A similar behaviour is observed for an airfoil with GF and a delta wing with GF.

The presence of the LES did not change the slope of the lift coefficient from a 0° to a 30° angle of attack. The 1.5% c and 3% c LES delayed the RDW stall angle by 5 degrees and

7.5 degrees respectively, as illustrated in Figure 21. The presence of the LES did not change the slope of the lift coefficient.

4.1.2 Drag coefficient

The RDW drag is also compared with the DW drag at all angles of attack, as illustrated in Figure 22. At lower angles of attack (i.e. $\alpha < 18^o$), the DW drag is comparably smaller. This is due to flow separations at the leading edge of the RDW. This separated flow will roll up at the wing's leading edge and form a spanwise vortex (or SV).

This SV breaks down due to the interaction of the SV and the boundary layer flow over the wing's top surface. The breakdown of the SV will result in a large separated flow region over the wing surface, dramatically increasing the pressure drag. The size of the separated flow region will also expand in size if the angle of attack increases, as illustrated in Figure 26.

On the other hand, the flow also separated at the DW leading edge at this range of angle of attack (i.e. $\alpha < 18^o$). Unlike a RDW, the flow separated from the leading edge of the DW forms a pair of stable counter rotating vortices with a strong jet-like vortex core. Hence, no dramatic pressure drag increase occurs for the DW with an increasing angle of attack (for $\alpha < 18^o$).

As the angle of attack increases over 18°, the DW drag is greater than the RDW drag. The DW drag increase may be due to the occurrence of LEV breakdown introduced at a low axial speed flow in the vicinity of the trailing edge of the wing starting at about 18 degrees of incidence [44]. The presence of the wake-like vortex core may increase the pressure drag of the DW. The drag produced by the RDW amplifies with an increasing SES height at all angles of

attack. The reason for such an increase in drag may be because of the presence of SES acts as a bluff body when attached to the sides of the RDW.

4.1.3 Lift over drag verses lift coefficient and drag polar

The L/D ratio is plotted in Figure 23 against all the lift coefficients. Figure 23 shows the increase in drag caused by the presence of the SES. The RDW does not overshadow the increase in lift increments at a medium to high lift coefficient. The SES consequently boosts the aerodynamic performance of the RDW. The drag polar (Figure 24) indicates that the RDW with SES has a lower drag coefficient at the same level of lift coefficient regardless of the strip heights. The reason for this could be traced back to the lift coefficient plot (Figure 21). The lift plot suggests that the baseline RDW has to be positioned at a much higher angle of attack to generate the same lift as the RDW with SES (see Figure 21 black dotted line). As mentioned earlier, the size of the separated flow region also enhances as the angle of attack increases, in turn generating a higher pressure drag.

4.2. Variation of vortex characteristics in the streamwise direction

In this section, detailed analyses of the flow field of a baseline reverse delta wing (RDW) were carried out at $\alpha = 18^o$. A flow field survey for a conventional delta wing (DW) is also completed at the same angle of attack. The purpose of this investigation is to make a comparison between the vortex characteristics of a RDW and the leading edge vortices (LEVs) of a DW at the same angle of attack. Flow field scans were carried out using a seven-hole pressure probe (SHP) at several chordwise locations from x = 0.2 c to 1.5 c with an increment of 0.1 c

The composite iso-vorticity contours, a quantitative representation of the tip vortex evolution of a RDW are in comparison with the evolution of the DW LEVs at $\alpha = 18^o$. This is exhibited in Figure 27 (a). The LEVs, also called the primary vortices generated by a DW, generally have higher peak vorticity than a RDW before the vortex breakdown. The RDW's vortex tip resembles an "arm and fist" structure (see Figure 25). In contrast to the DW LEVs, the RDW's tip vortices are located away from the wing surfaces, which suggest they do not provide suction forces over the wing's surface.

The LEV shear layer has a higher vorticity value than the arm generated by the RDW at all the chordwise stations (Figure 27). This may indicate a stronger roll-up process for the DW vortex. For both the RDW and DW, the arm and shear layer are growing in size in the chordwise direction. Near the trailing point of the RDW, the arm of a tip vortex generated by RDW is interacting with the low speed separated flow region over the wing surface. The increase in the size of the RDW arm may be due to this interaction.

Figure 28 (a and b) show the core location of the vortex core of both the DW and the RDW, which further reveals the vortex trajectory for both configurations. The DW LEV core location is vertically closer to the wing's surface than a RDW tip vortex (see Figure 28 (b)).

Figure 28 (c) shows that the DW's primary vortex gradually decreased in their peak vorticity from x/c values of 0.3 to 0.8, a sudden drop of the peak vorticity value for the primary vortex can be observed at x/c = 0.8. It is worth mentioning that at the same location, the core axial velocity immensely decreased (see Figure 28 (g)) to a value lower than the free stream and the $v_{\theta_{max}}/U$ (shown in Figure 28 (d)) decreased sharply. All these trends of the important flow

41

field parameters indicate that the LEV breakdown occurred at a location between x/c = 0.8 to x/c = 0.9.

Figure 28 (e) shows that the RDW tip vortices radiuses versus the wing chordwise direction. The core radius is obtained by finding the distance between the vortex core and the location circumferential averaged $v_{\theta_{max}}$. This figure shows that the RDW tip vortices do not undergo sudden expansion at any locations in the wing's streamwise direction. Instead, the vortex gradually gains vortex core size as it evolves downstream. The gain in size of the vortex is associated with a gradual drop in the peak vorticity value (see Figure 28 (c)). This may explain that the RDW's tip vortices do not breakdown as they evolve downstream, instead, the vortex undergoes diffusion. The diffusion of the vortex may be due to the interaction of the vortical flow and the separated flow over the wing's surface. Figure 28 (c) shows the vortex core peak vorticity generated by both wings. The DW core peak vorticity has a much higher value than the RDW at all locations. Figure 28 (d) also illustrates that the maximum tangential velocity of the DW LEV is much higher than the RDW tip vortices at any chordwise locations. The data stated above indicate the LEV is more concentrated compared to a tip vortex generated by a RDW at the selected angle of attack.

4.3. Variation of vortex characteristics in the streamwise direction as a function of angle of attack

This section will discuss the chordwise vortex evolution of a baseline RDW at different angles of attack. The purpose of this investigation is to gain a better understanding of the behaviour of the RDW's tip vortices. As mentioned earlier, the RDW's tip vortex diffuses while it evolves downstream. This section will explain the cause of the vortex diffusion. Moreover, it is

important to understand the flow behaviour over the top surface of the RDW. Therefore, the flow structure to the top RDW's surface is provided by flow visualization.

4.3.1 Composite iso-vorticity contours

Figure 25 shows the structure of the RDW's vortex at a 10 degree incidence and x/c = 0.9. As mentioned before, the vortex is located away from the wing's surface with a "vortex arm" connecting the vortex to the wing. This "arm" is the result of the interaction between fluid particles escaping from the bottom of the wing's surface and the low speed separated flow over the wing's surface.

Composite iso-vorticity contours (Figure 29 – 32) again show that the RDW's vortices are not located directly above the wing's surface at any chordwise locations at any incidences. The vortex trajectory suggests that no vortex lift is generated over the RDW at any angle of attack. The radius of the vortex and the arm thickness is increasing as the vortex evolves in the chordwise direction. This change in vortex size is associated with the RDW vortex undergoing diffusion while it evolves downstream.

The vortex arm suggest the exchanging momentum between the arm and the separated flow over the RDW's top surface. The RDW vortex undergoes further diffusion while it evolves downstream as the angles of attack increase. For a better understanding of the RDW vortex diffusion, dye flow visualization is carried out to provide a better qualitative understanding of the flow structure around the wing.

4.3.2 Dye flow visualization

The results suggests that the diffusion of the RDW vortex is the result of interaction of the vortical flow and the separated flow over the wing. The flow visualization can provide a qualitative understanding for the interaction between the vortical flow structure and the separated flow.

Figure 33 (b) shows that the vortex generated by the wing at $\alpha = 10^o$ is very concentrated. The side view indicates that the size of the separated flow region is small and the influence of separated flow is very small in regards to the RDW tip vortices, where the latter are located horizontally, far away from the wing surface.

Figure 33 (c) Shows that when the wing is positioned at a 20 degree angle of attack the size of the separated flow region is increased under the comparison. Figure 33 (d) demonstrates that the vortex trajectory is moving closer to the RDW's center line and the vortex undergoes diffusion while it evolves downstream. This indicates the vortical flow and separated flow interaction occurs.

Around the stalling angle, at a 35 degree incidence the top view picture shows the dye injected from the tip of the wing is mixed with the flow over the wing's surface. The mixing of the dye injected from the tip of the RDW suggests very strong interaction between the vortical flow and the separated flow over the wing.

4.3.3 Important vortical flow quantities

Figure 34 (a) is the plot of the core axial velocity against chordwise locations at different angles of attack. One could notice that all the core axial velocities are increasing marginally with

an increasing chordwise distance. This suggests that the gain in total circulation strength of the vortex (see Figure 34 (e)) is balanced by the increasing rotational forces of the vortex. The gain of the rotational forces is provided by the increase in pressure differences between the center of the vortex core and the flow region outside of the vortex. Therefore, the gain in total circulation strength in the chordwise direction will lead to a reduction in core static pressure and results in core axial flow acceleration.

Figure 34 (a) also indicates the vortex core is weak and jet-like at $\alpha = 10^o$. The overall axial core velocity is decreasing with an escalating angle of attack. The RDW vortex core is wake-like when the wing is positioned at $\alpha = 22^o$. The lower-than-freestream velocity is observed at locations throughout the chordwise locations. The formation of a wake-like core may be due to the vortex entraining the separated flow over the wing's surface at locations very close to the leading edge.

The directly measured maximum tangential velocity has been plotted against the wing's chordwise direction at different α (see Figure 34 (c)). The $v_{\theta_{max}}/U$ start to decrease from a location around x/c = 0.5 as chordwise distance increases. Figure 34 (b) shows that the circumferential averaged core radius, which is defined by the distance between the maximum tangential locations and the location of the vortex center, augments as the chordwise distance increases. The observation is associated with a drop in peak vorticity values (see Figure 34 (d)). The decrease of the maximum tangential velocity, gain in core size and the drop in vortex peak vorticity values could be explained by the vortex is being diffused by the separated flow over the wing's surface.

The three aforementioned quantities has also compared at a selected chordwise location with increasing in angle of attack. The rise of the $v_{\theta_{max}}/U$ associated with an increase in Γ_o indicates the wing bottom surface pressure increases with an α. The drop of peak vorticity value and the rise of the vortex core radius indicates the influence of the separated flow region to the vortex is increasing as the α increases.

The rise in the maximum tangential velocity in the vicinity of the leading edge indicates that the rotation speed of the core is increasing for a fraction of the chord distance (as illustrated in Figure 34 (c)). This fraction of the chord distance could be called the "vortex formation distance". It is suggested by Altaf et al. [3]'s CFD simulation that the formation of the RDW's tip vortices is triggered by the formation of the SV. According to the vorticity transport theorem, the acceleration in the SV vorticity in the chordwise direction is stretched due to the presence of the flow velocity gradient. This acceleration of the SV vorticity is transferred to the angular acceleration of the RDW tip vortices' tangential velocities. Therefore, the chordwise distance between the peak maximum tangential locations and the leading edge could suggest the diameter of the SV. However, the SV radius of the RDW positioned at $\alpha = 10^o$ cannot be clearly identified. This may be due to the size of the SV at $\alpha = 10^o$ is very small which falls into the experimental uncertainty. The SV radius for 14, 16, 18 and 22 degrees of incidence are 0.15 c, 0.3 c, 0.3 c, 0.4 c, respectively.

4.4. Reverse delta wing vortex evolution and control

In this section, a detailed analysis of the RDW vortex evolution is performed along all the chordwise locations for a RDW with two different side edge strip (SES) heights (1.5% c and 3% c) and 3% c leading edge strip (LES).

It is important to enhance the RDW lift by SES since the lift generated by the RDW is much less compared to the DW, which is discussed in Section 4.1 and 4.2. As described in the previous section, the birth of the baseline RDW tip vortices are associated with the formation of the SV. Passive control devices such as the leading edge strips (LES) are used to control the SV formation structure and/or modify the wing's aerodynamic performance, such as delaying the stall. For the purpose of the flow structure investigation, a 14 degree angle of attack is chosen for the wing with all three control devices due to the size of the vortex and the shape of the vortex remains fairly circular.

4.4.1 Side-edge strip

Figure 35 shows the iso-vorticity contours for a RDW with 1.5% c and 3% c SES. The iso-vorticity contours generated by the wing with SES are directly compared to the iso-vorticity contours generated by the baseline RDW. One could notice that the vortex arm thickness and the arm vorticity value of the RDW with SES is slightly lower when compared to the arm of the BW RDW. This suggests that the SES is introducing a spanwise blockage to the fluid particles to reduce the particle escaping velocity.

Due to the presence of the SES, the adverse pressure gradient near the wing's side edge may increase in both the chordwise and the spanwise direction of the wing, thus resulting in a higher speed of flow separation at the leading edge of the RDW, as well as a moment being imposed onto the flow field in both the spanwise and chordwise direction. The stronger leading edge separation leads to a stronger SV formation. The strong SV will resist breakdown over the wing's top surface. This could lead to a reduction in separated flow region size. The reduction in the RDW's separated flow region size is evidenced by iso-axial flow contours plotted at x/c = 1.01 (Figure 36).

47

The aforementioned moment imposed by the SES to the flow field could be observed from Figure 38 (d), where a downward shift of the vortex core location is observed. The downward shift of the vortex core is increasing with increases in the SES height. Thus, explaining the adverse pressure gradient increase with a growing strip height.

Other critical vortex flow field quantities have been plotted in Figure 38, the vortex generated by the RDW with 3% c SES has the highest peak vorticity values at any chordwise locations compared to the BW RDW Figure 38 e). The peak vorticity values rise with increasing SES heights at all the chordwise locations. Based on the circumferential averaged vortex radiuses, the vortex generated by the RDW with 1.5% c SES is smaller when compared to the BW RDW at any chordwise locations (Figure 38 (a)). Vortices generated by the RDW with 3% c SES have a slightly higher radius compared to a BW RDW. That is, the vortex generated by the wing with 1.5% c and 3% c SES are more concentrated compared to the vortex generated by a baseline RDW at all the x/c locations tested.

The presence of the SES led to an increased directly measured maximum tangential velocity increase (Figure 38 (b)) the presence of SES. The shift is growing with an increasing SES height. Figure 38 (b) also shows that the radius of the SV generated by the RDW with 1.5% c and 3% c SES cannot be determined since the increase in the maximum tangential velocity in the chordwise direction cannot be observed. The reason for this might be due to the resolution in the chordwise scans ($\Delta x/c = 0.1$), which suggests that the size of the SV is tiny for the wing with control surfaces.

Figure 38 (c) describes the core axial velocity plotted against the chordwise location. The core axial velocities are obtained by using the axial velocities at peak vorticity values locations

of the vortices. In comparison to the BW RDW, the vortex generated by the wing with SES has a wake-like core. The vertical trajectory of the vortex (see Figure 38 (d)) suggests that the can entrain low speed flow particles downstream of the SES.

4.4.2 Leading-edge strip

The downward deflected leading-edge strip (LES) can delay the stall and improve the post stall lift generation, which is evidenced from Figure 21. It suggests that the LES modifies the pressure distribution over the RDW's top surface at higher angles of attack.

Iso-vorticity contours at different streamwise locations have been plotted in Figure 39. The results are directly compared to the data from the BW RDW. It is obvious that the peak vorticity value is higher for the vortex generated by the BW RDW in comparison. Unlike the SES, the LES should not provide spanwise blockage to the flow at the bottom surface of the wing. The vorticity values suggests that the LES could disturb the flow on the bottom surface of the wing. Important vortex flow quantities have been plotted against the wing's chordwise locations to prove this.

Figure 37 b) shows the maximum tangential velocity of the RDW vortex plotted against the wing's chordwise locations. As illustrated, the maximum tangential velocity is smaller than the tangential velocities of the RDW's tip vortices. A decrease in peak vorticity (see Figure 37 (c)) associated with an increase in the circumferential averaged core radius (see Figure 37(a)) is also observed. The behaviour of the core radius and the peak vorticity values indicates that the vortex is less concentrated compared with the vortex generated by the BW RDW. The formation of the vortex is the result of the interaction between the vortex and the separated flow over the top of the wing's surface, as described previously.

49

4.5. Variation of the vortex characteristics with angles of attack

Figure 40 shows the growth of the BW RDW vortex and the growth of the vortex generated by the RDW with 3% c SES at chordwise stations x/c = 1.01 for $\alpha = 4^o - 28^o$. The iso-vorticity contour plot shows that the vortices and the vortex arms continuously grow in size for both configurations with increasing angles of attack. At high angles of attack ($\alpha > 24^o$), the contour lines become very disordered for both the tip vortices and the arm in regards to both wing configurations. This indicates the vortex is diffused at the given location and the given angle of attack. At low angles of attack ($\alpha < 12^o$), the vorticity values for the vortex arm is lower for the RDW with 3% c SES, which indicates that the strips introduce blockage to the fluid particles escaping from the wing's bottom surface at low angles of attack. The vortex generated by both wing configurations however remains concentrated.

Important vortical flow quantities have been plotted against angles of attack in Figure 41. We can notice that the vertical core locations are lower for the RDW with SES at all the angles of attack. The core axial velocity is decreasing as the angle of attack increases for both wing configurations. The core axial velocity switch from weak-jet-like to wake-like for BW RDW starting at $\alpha = 14^o$.The plot shows the vortex generated by the RDW with 3.0% c SES has a wake-like core at all the angles of attack tested in this study.

The vortex's directly measured maximum tangential velocity for the BW RDW is increasing until around $\alpha = 14^o$ while the maximum tangential velocity of the vortex generated by the RDW with 3% c SES is higher than the BW RDW at all the angles of attack tested.

50

The vortex core radiuses, which is determined based on circumferential averaged results are roughly the same for both configurations at all the angles of attack tested. The vortex core radius does not increase with increasing angles of attack until around $\alpha = 14^o$ for both wing configurations. The vortex core radius expands immensely for both configurations with increasing α for $\alpha = 14^o$. The vortex peak vorticity values increase also to a maximum at roughly a 14 degree incidence level for both configurations. The peak vorticity value then decreases after it reaches its maximum as the angle of attack increases. The trend of maximum tangential velocity, peak vorticity and core radius suggests that the vortex is concentrated for both configurations for $\alpha < 14^o$. At a higher incidence, vortices generated by both configurations are diffused due to a massive increase in core radius as well as a drop in peak vorticity values.

5. Conclusions

5.1. DW and RDW aerodynamics

a) The RDW generated less lift compared to a DW at the same angle of attack, whereas the stalling angle remained about the same.

b) The RDW with SES can boost the lift significantly from a 0 to a 40 degree angle of attack. However it decreases the stalling angle slightly.

c) The increment of the lift increase enlarges with increasing SES heights.

d) The LES can boost the wing's post-stall performance and delay the wing stall by approximately 5 degrees.

e) The increment in the increasing post stall lift generation enlarges with growth in LES heights.

f) The increase in the lift generation by the wing with SES is associated with a moderate drag increase.

g) The SES can increase the RDW lift-to-drag ratio at a certain lift coefficient.

h) The drag polar indicates that the RDW with SES can reduce the drag at the same lift coefficient.

5.2. Flow field investigation

5.2.1 DW and RDW at $a = 18^o$

a) The trajectory of the vortex indicates that the vortex generated by the DW is closer to the wing surface and located inboard over the wing.

b) The RDW tip vortices are located outside of the wing's surface. This suggests that the RDW vortices do not provide lift to the wing.

c) The LEV core axial velocity of the DW is higher than the RDW core axial velocity before breakdown.

d) The tip vortices generated by the RDW does not breakdown. Instead, it expands gradually along its chordwise direction associated with a gradual peak vorticity drop.

e) The LEVs generated by the DW are stronger than the tip vortices generated by the RDW.

f) Prior to breakdown, the LEVs are more concentrated compares to RDW tip vortices.

5.2.1 Baseline reverse delta wing

a) The arm of the vortex grows in size with increasing streamwise distance.

b) The overall core axial velocity decreases with increasing angles of attack.

c) The RDW's tip vortices are being diffused while they are evolving downstream. This is confirmed by observing the peak vorticity trend and the expansion of the core radius.

d) The vortex would become less concentrated at higher angles of attack.

e) The formation of the SV is associated with the formation of the RDW tip vortices.

5.2.2 Reverse delta wing with passive control surfaces

a) The vortex generated by the RDW with SES is more concentrated when compared with a Baseline RDW.

b) A downward vortex center location is detected due to a restriction provided by the SES to the fluid particles escaping from the wing bottom surface, consequently an increase of bottom wing surface pressure.

c) The vortex generated by the RDW with SES always has a wake-like core.

d) The RDW with LES can generate a more diffused vortex compared with a baseline RDW.

e) No obvious vortex core location changes is observed under the comparison between a baseline RDW and a RDW with LES.

5.2.3 Variation of vortex characteristics with angles of attack

a) The vortex generated by the BW RDW has a weak-jet-like core from angles of attack ranging from 4 to 14 degrees. The vortex is becoming wake-like with increasing in angle of attack furthermore.

b) The peak vorticity values increases until the angle of attack is 14 degrees and starts to decrease due to the vortex undergoes diffusion for both wing configurations.

c) The sudden increase in the vortex core radius, sudden decrease in vortex peak vorticity values at 14 degrees angle of attack.

6. Recommendations for future work

a) Hot wire could be used to understand the relationship further between the wake region and the vortex.

b) A RDW with pressure tabs could be used to understand the pressure distribution over and under the wing surface.

c) Similar experiments could be performed with a different Reynolds number.

d) A RDW with different sweeping angles can be tested to understand the relationship between the wing aerodynamic performance and the wing's sweeping angle.

e) The size of the SV could be determined experimentally by using particle imaging velocimetry (PIV).

References

[1]   A. M. Mitchell, and J. Délery, "Research into vortex breakdown control," *Progress in Aerospace Sciences,* 2001, vol. 37, no. 4, pp. 385-418.

[2]   E. C. Polhamus, "Predictions of vortex-lift characteristics by a leading-edge suction analogy," *Journal of Aircraft,* 1971, vol. 8, no. 4, pp. 193-199.

[3]   A. Altaf, A. A. Omar, W. Asrar, and H. B. Jamaluddin, "Study of the reverse delta wing," *Journal of Aircraft,* 2011, vol. 48, no. 1, pp. 277-286.

[4]   I. Gursul, Z. Wang, and E. Vardaki, "Review of flow control mechanisms of leading-edge vortices," *Progress in Aerospace Sciences,* 2007, vol. 43, no. 7–8, pp. 246-270.

[5]   R. C. Nelson, and A. Pelletier, "The unsteady aerodynamics of slender wings and aircraft undergoing large amplitude maneuvers," *Progress in Aerospace Sciences,* vol. 39, no. 2–3, pp. 185-248, 2003.

[6]   E. C. Polhamus, "A concept of the vortex lift of sharp-edge delta wings based on a leading-edge-suction analogy,*" NASA technical note*, National Aeronautics and Space Administration: Washington, D.C., 1966.

[7]   L. W. Traub, and S. F. Galls, "Effects of leading- and trailing-edge Gurney flaps on a delta wing," *Journal of Aircraft,* 1999, vol. 36, no. 4, pp. 651-658.

[8]   M. Gad-El-Hak, and R. F. Blackwelder, "The discrete vortices from a delta wing," *AIAA Journal,* 1985, vol. 23, no. 6, pp. 961-962.

[9]   C. Breitsamter, "Unsteady flow phenomena associated with leading-edge vortices," *Progress in Aerospace Sciences,* 2008, vol. 44, no. 1, pp. 48-65.

[10]   S. Kaplan, and A. Altman, "Wake vorticity measurements for low aspect ratio wings at low reynolds number," *Journal of Aircraft,* 2007, vol. 44, no. 1, pp. 241-251.

[11]   R. C. Nelson, and K. D. Visser, "Breaking down the delta wing vortex," *University of Notre Dame*, Notre Dame, Indiana, 1990.

[12]   M. V. Lowson, and A. J. Riley, "Vortex breakdown control by delta wing geometry," *Journal of Aircraft,* 1995, vol. 32, no. 4, pp. 832-838.

[13]   Q. Deng, and I. Gursul, "Effect of leading-edge flaps on vortices and vortex breakdown," *Journal of Aircraft,* 1996, vol. 33, no. 6, pp. 1079-1086.

[14]   I. Gursul, "Unsteady flow phenomena over delta wings at high angle of attack," *AIAA Journal,* 1994, vol. 32, no. 2, pp. 225-231.

[15]   D. M. Rao, "Leading edge vortex-flap experiments on a 74 deg delta wing," Technical Report, *Old Dominion Univsity*, Norfolk, VA, 1979.

[16]   Q. Deng, and I. Gursul, "Vortex breakdown over a delta wing with oscillating leading edge flaps," *Experiments in Fluids,* 1997, vol. 23, no. 4, pp. 347-352.

[17]   N. C. Lambourne, and D. W. Bryer, "The bursting of leading-edge vortices - some observations and discussion of the phenomenon," *Aeronautical Research Council Reports and Memoranda*, Ministry of Aviation: London, United Kindom, 1961, no. 3282.

[18]   J. W. H. Wentz, and D. L. Kohlman, "Vortex breakdown on slender sharp-edged wings," *Journal of Aircraft,* 1971, vol. 8, no. 3, pp. 156-161.

[19]   F. M. Payne, "Structure of leading-edge vortex flows including vortex breakdown," Ph.D. Dissertation, *University of Notre Dame*, Notre Dame, Indiana, 1987.

[20]   G. E. Erickson, "Water-tunnel studies of leading-edge vortices," *Journal of Aircraft,* 1982, vol. 19, no. 6, pp. 442-448.

[21]   Y. Li, and J. Wang, "Experimental studies on the drag reduction and lift enhancement of a delta wing," *Journal of Aircraft,* 2003, vol. 40, no. 2, pp. 277-281.

[22]   L. W. Traub, "Effects of anhedral and dihedral on a 75-deg sweep delta wing," *Journal of Aircraft,* 2000, vol. 37, no. 2, pp. 302-312.

[23]   R. Nangia, and G. Hancock, "Delta wings with longitudinal camber at low speed," *Queen Mary colledge*, Univsersity of London, United Kindom, 1970.

[24]   H. E. Helin, and C. W. Watry, "Effects of trailing-edge jet entrainment on delta wing vortices," *AIAA Journal,* 1994, vol. 32, no. 4, pp. 802-804.

[25]   C.H. Kuo, and C. W. Hsu, "Development of vortical structure over delta wing with leading-edge flap," *Journal of Aircraft,* 1997, vol. 34, no. 5, pp. 577-584.

[26]   K. Rinoie, "Experiments on a 60-degree delta wing with rounded leading-edge vortex flaps," *Journal of Aircraft,* 2000, vol. 37, no. 1, pp. 37-44.

[27]   S. Oh, and D. Tavella, "Analysis of a delta wing with leading-edge flaps," *Journal of Aircraft,* 1987, vol. 24, no. 6, pp. 353-354.

[28]   J. F. Marchman III, "Aerodynamics of inverted leading-edge flaps on delta wings," *Journal of Aircraft,* 1987, vol. 18, no. 12, pp. 1051-1056.

[29]   C. S. Reddy, "Spanwise pressure distribution on delta wing with leading-edge vortex flap," *Journal of Aircraft,* 1987, vol. 24, no. 3, pp. 222-224.

[30]   D.I. Greenwell, "Gurney flaps on slender and non-slender delta wings," *journal of aricraft*, 2010, vol. 47, no.2, pp 675-681.

[31]   M. D. Buchholz, and J. Tso, "Lift augmentation on delta wing with leading-edge fences and Gurney flap," *Journal of Aircraft,* 2000, vol. 37, no. 6, pp. 1050-1057.

[32]   L. W. Traub, "Aerodynamic characteristics of spanwise cambered delta wings," *Journal of Aircraft,* 2000, vol. 37, no. 4, pp. 714-724.

[33]   H. Winter, "Strömungsvorgänge an platten und profilierten körpern bei kleinen spannweiten," *Forschung auf dem Gebiet des Ingenieurwesens,* 1935, vol. 6, no. 2, pp. 67-71.(In English)

[34]   L. W. Traub, "Aerodynamic characteristics of vortex flaps on a double-delta planform," *Journal of Aircraft,* 1995, vol. 32, no. 2, pp. 449-450.

[35]   V. J. Rossow, "Lift enhancement by an externally trapped vortex," *Journal of Aircraft,* 1978, vol. 15, no. 9, pp. 618-625.

57

[36]   V. J. Rossow, "Two-fence concept for efficient trapping of vortices on airfoils," *Journal of Aircraft,* 1992, vol. 29, no. 5, pp. 847-855.

[37]   Y.Y. Niu, T.S. Hsu, C. T. Hsieh, C. C. Chang, and C. C. Chu, "How does a Gurney flap enhance the aerodynamics forces?," *AIAA Journal,* 2010, vol. 48, no. 11, pp. 2710-2714.

[38]   D. Jeffrey, X. Zhang, and D. W. Hurst, "Aerodynamics of Gurney flaps on a single-element high-lift wing," *Journal of Aircraft,* 2000, vol. 37, no. 2, pp. 295-301.

[39]   A. M. O. Smith, "High-lift aerodynamics," *Journal of Aircraft,* 1975, vol. 12, no. 6, pp. 501-530.

[40]   M. D. Maughmer, and G. Bramesfeld, "Experimental investigation of Gurney flaps," *Journal of Aircraft,* 2008, vol. 45, no. 6, pp. 2062-2067.

[41]   C. P. van Dam, D. T. Yen, and P. M. H. W. Vijgen, "Gurney flap experiments on airfoil and wings," *Journal of Aircraft,* 1999, vol. 36, no. 2, pp. 484-486.

[42]   R. Meyer, W. Hage, D. W. Bechert, M. Schatz, and F. Thiele, "Drag reduction on Gurney flaps by three-dimensional modifications," *Journal of Aircraft,* 2006, vol. 43, no. 1, pp. 132-140.

[43]   T. Lee, and Y. Y. Su, "Wingtip vortex control via the use of a reverse half-delta wing," *Experiments in Fluids,* 2012, vol. 52, no. 6, pp. 1593-1609.

[44]   W. J. Devenport, K.S. Wittmer, and C.W. Wenger, "*The spectral and statistical properties of turbulence generated by a vortex/blade-tip interaction,*" National Aeronautics and Space Administration, National Technical Information Service distributor, Blacksburg,VA, 1997.

Appendix
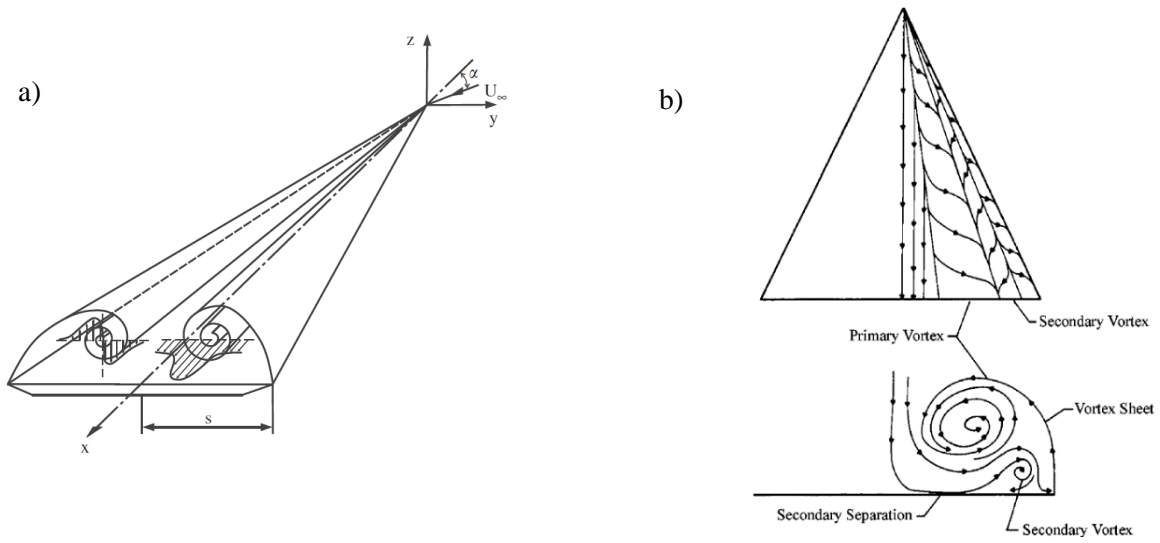
Figure 1 Schematic diagram for the leading-edge vortex, and b) LEV structure [5]
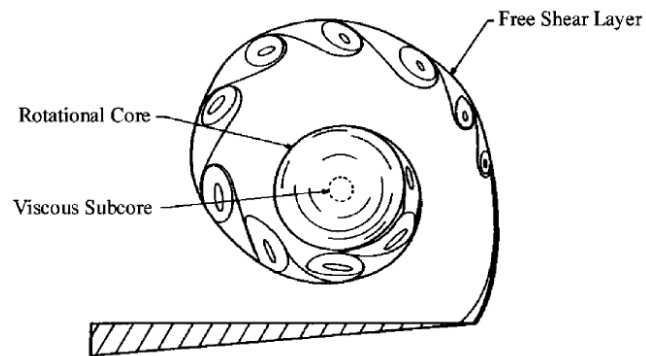
Figure 3 Leading-edge vortex with detail shear layer structure [1]
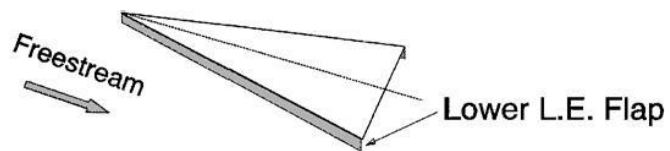
Figure 2 Leading-edge flap deflected downward [7]
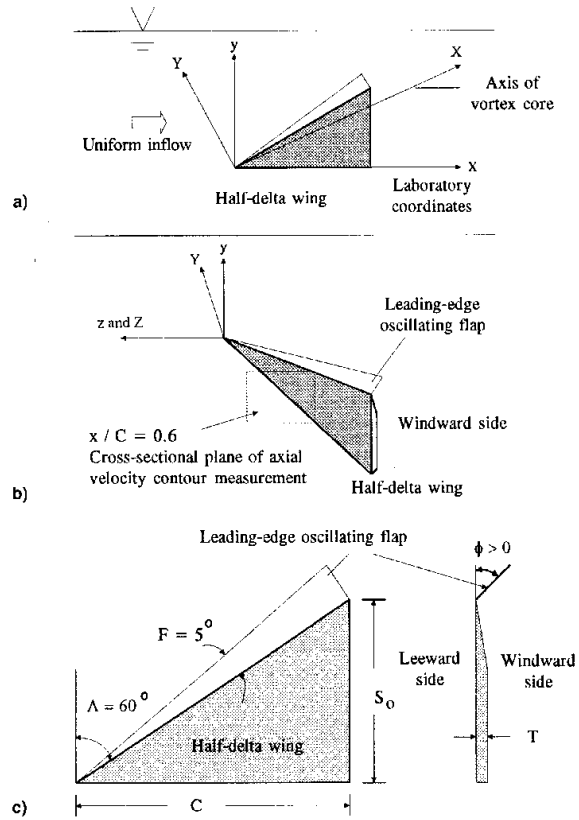
Figure 4 Leading-edge vortex flap (LEVF) [25]
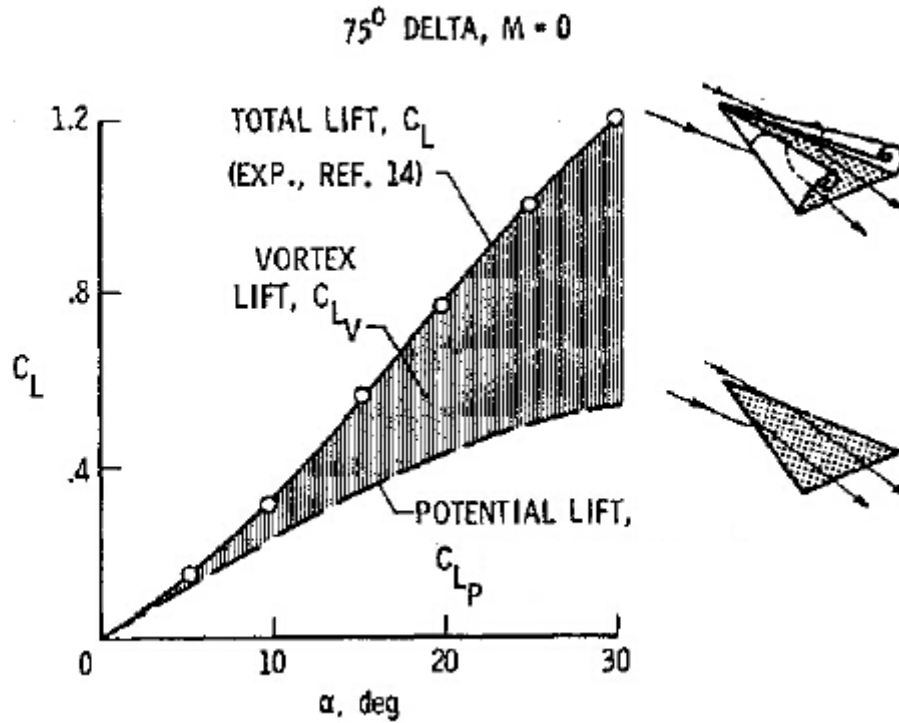
Figure 5 Delta wing potential lift and vortex lift [2]
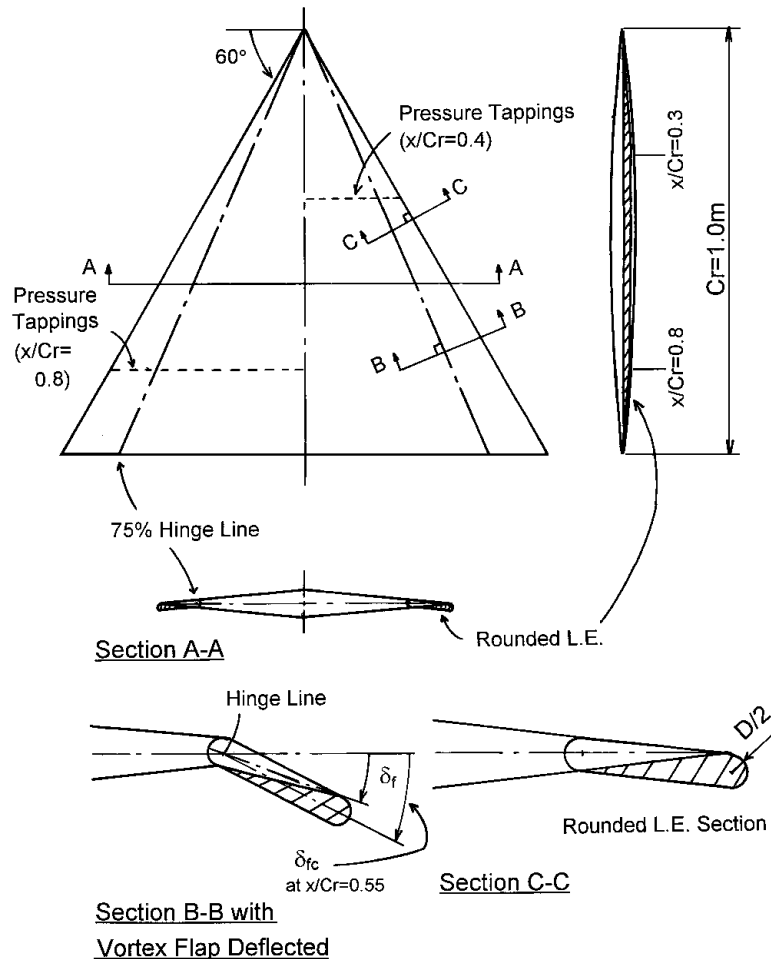
Figure 7 LEVF with rounded leading edge [26]
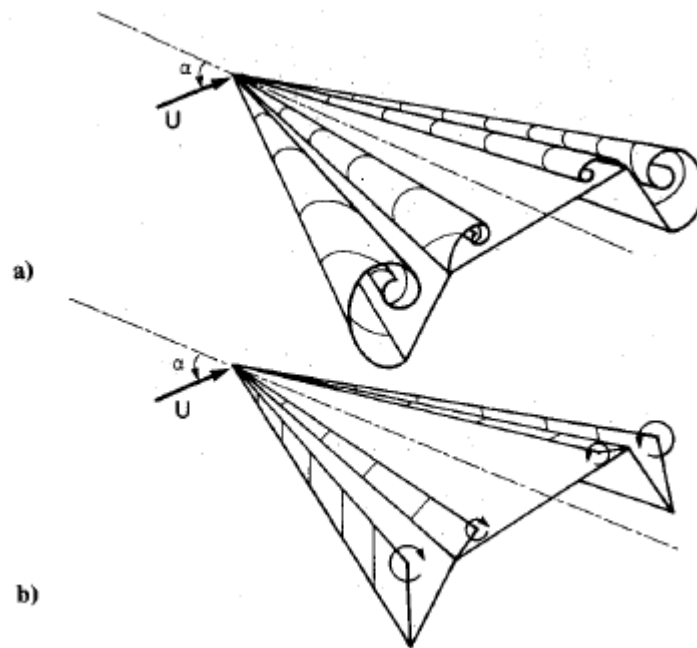
Figure 6 a) Conical delta wing with leading-edge flaps, and b) vortex-feeding-sheet model [27]
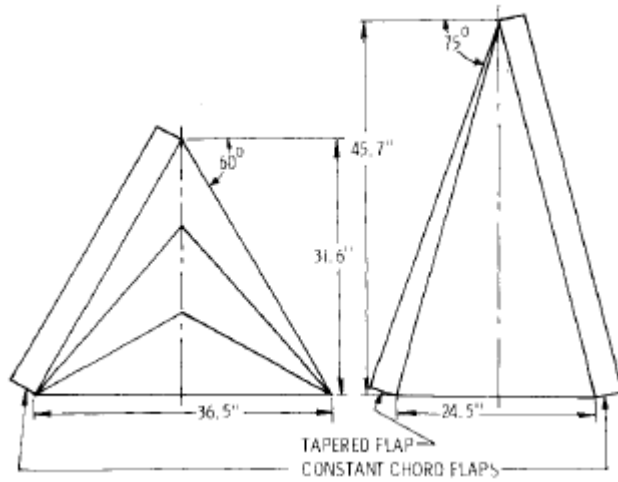
Figure 8 60-degree sweep delta wing (left) and 70-degree sweep (right) with LEF and fences [28]
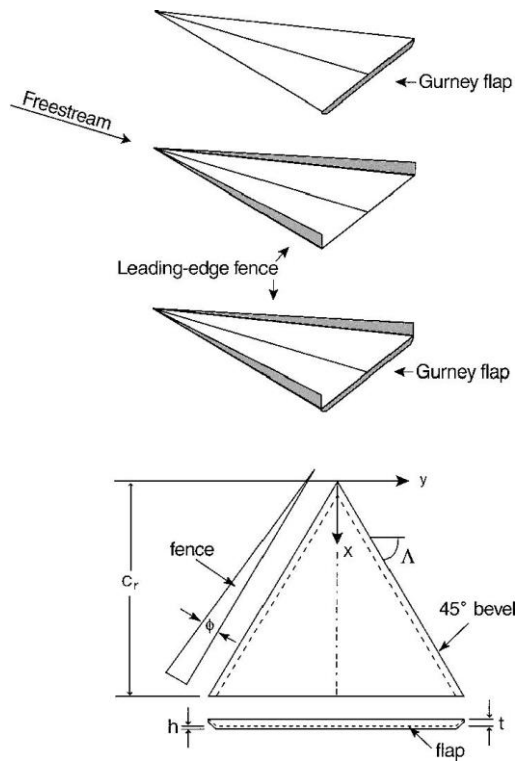
Figure 9 DW with leading-edge fences [31]
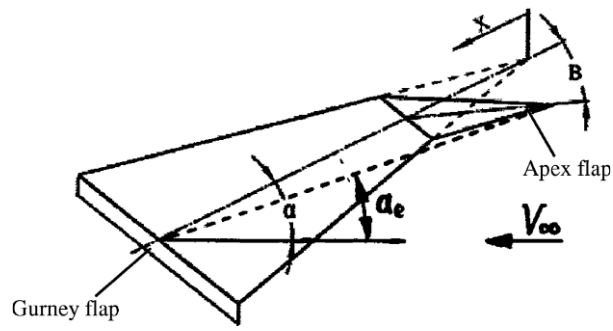
Figure 10 DW with GF and drooping apex [36]

a)   b)
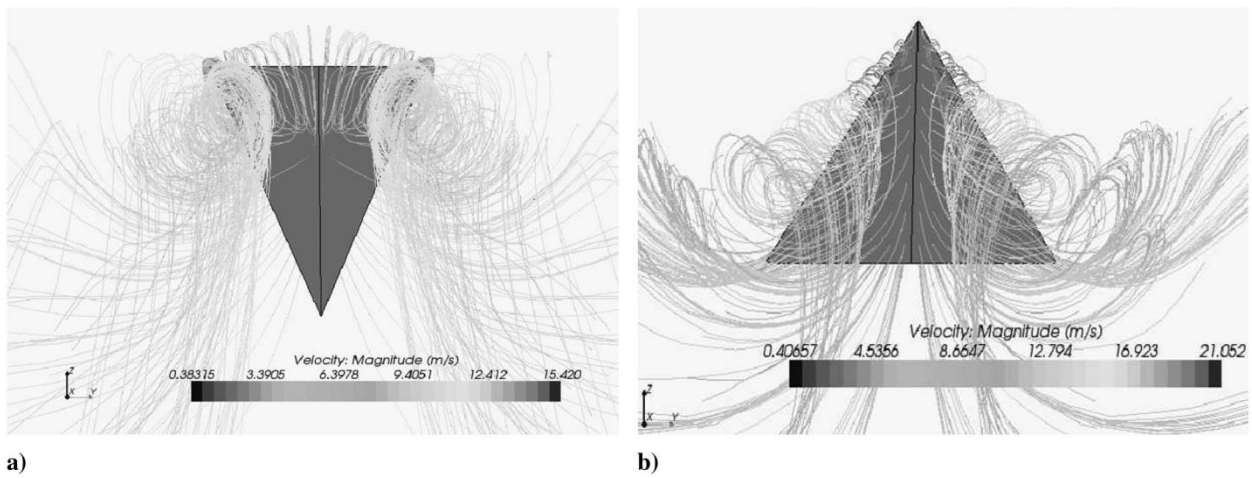
Figure 11 CFD simulation done by Altaf et al. [3]
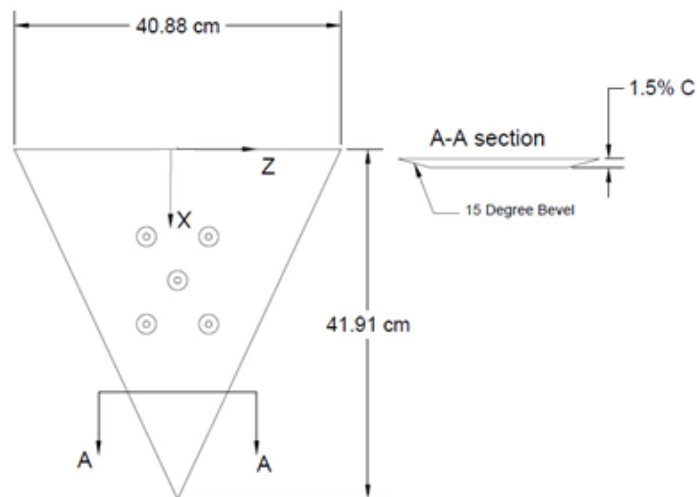
Figure 12 Reverse delta wing model
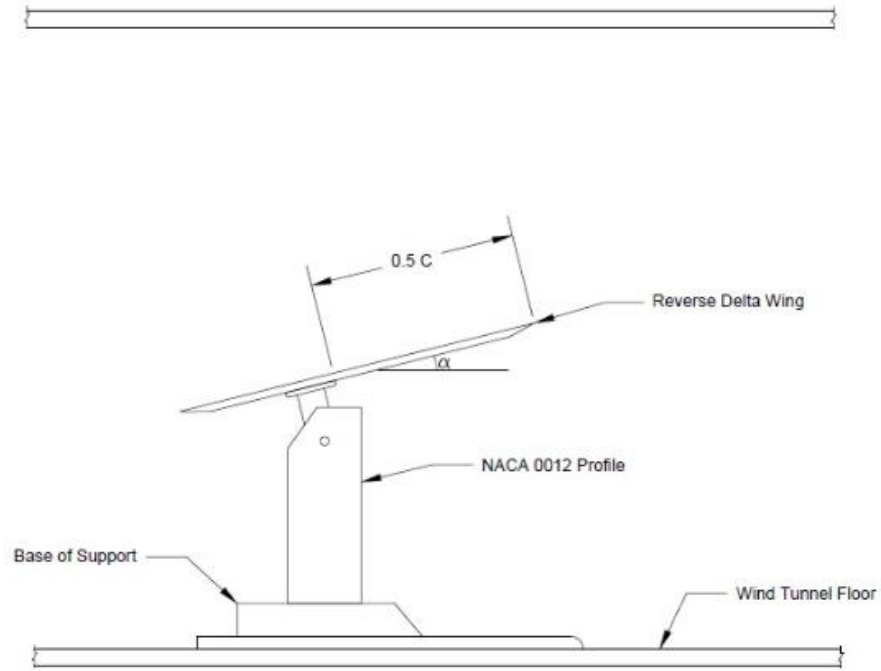
Figure 13 Schematic diagram of the support and wing
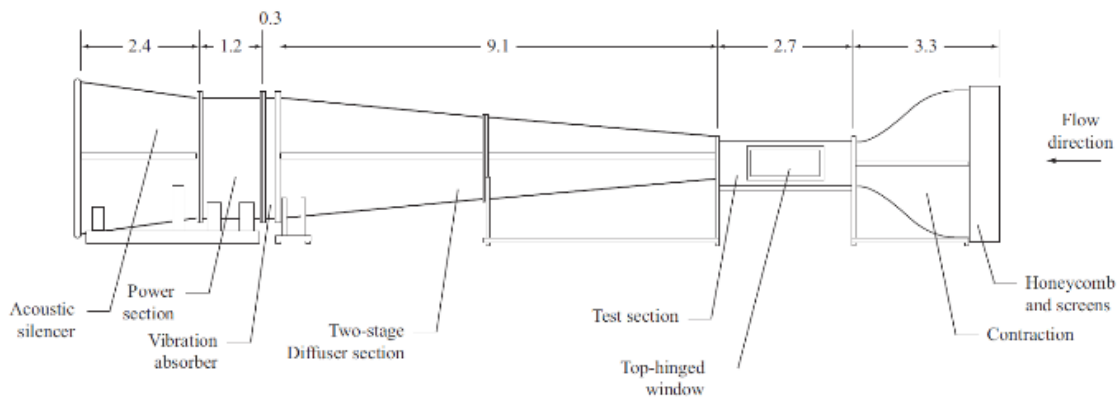
Figure 14 top) Schematic diagram of wind tunnel bottom left) Inlet of the wind tunnel, and bottom right) acoustic silencer of the wind tunnel
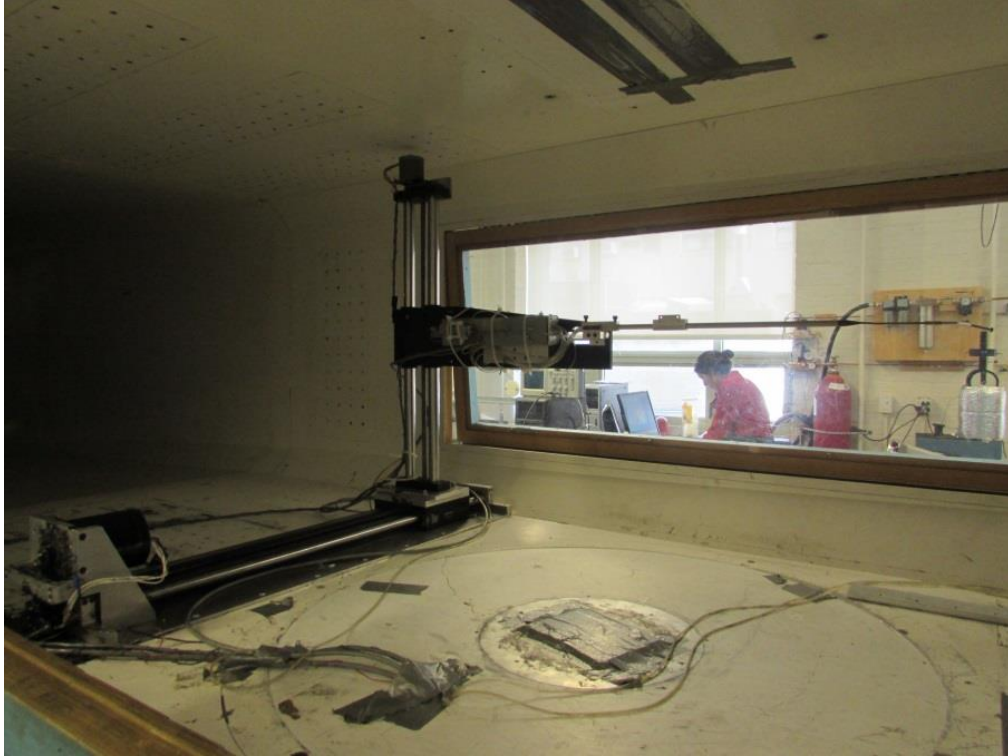
Figure 15 Traversing mechanism

Figure 16 Force balance set-up

a)

Turning Table

Cylinder Support

N

Airflow Direction

D

Y

L

α

Wind Tunnel Wall

b)

Reverse Delta Wing

Air Flow

Cylinder Support

Wind Tunnel Floor

Sensor Plate

Two-Component
Force Balance
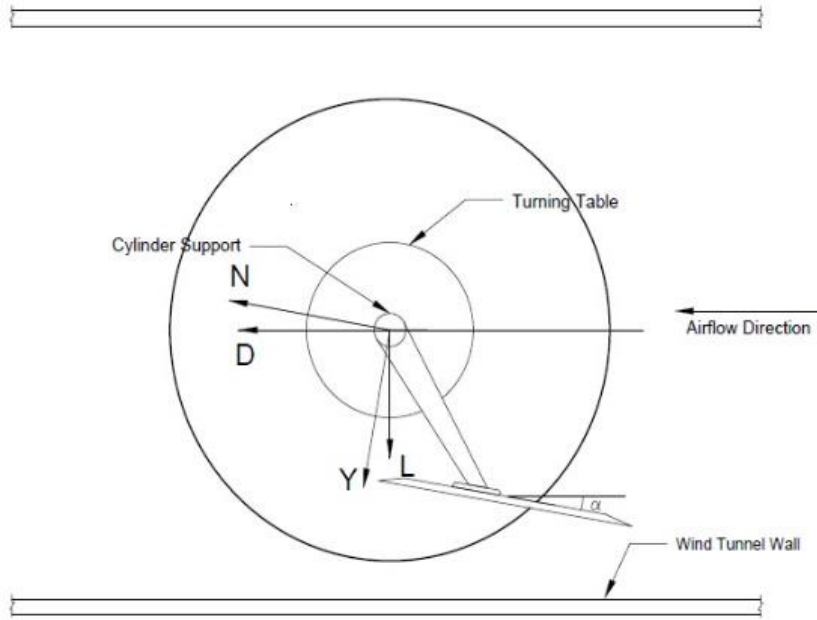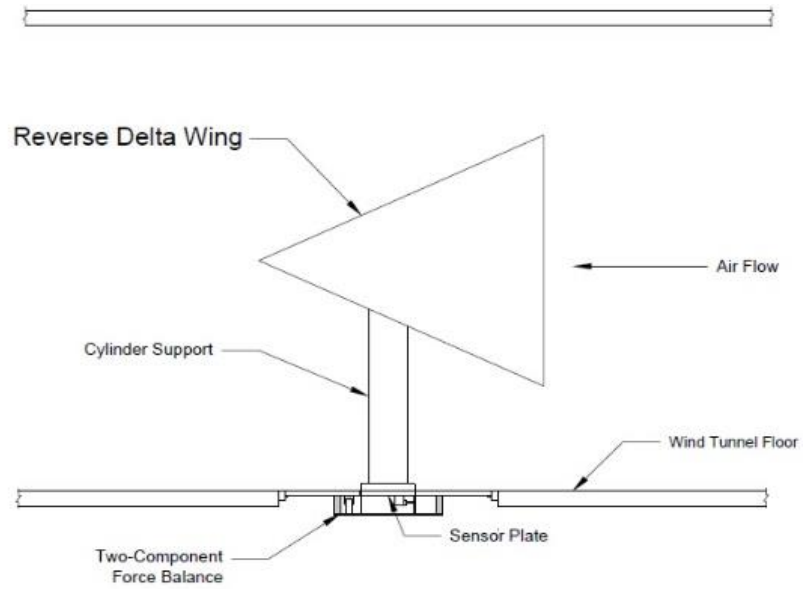
Figure 17 Schematic diagram of force balance
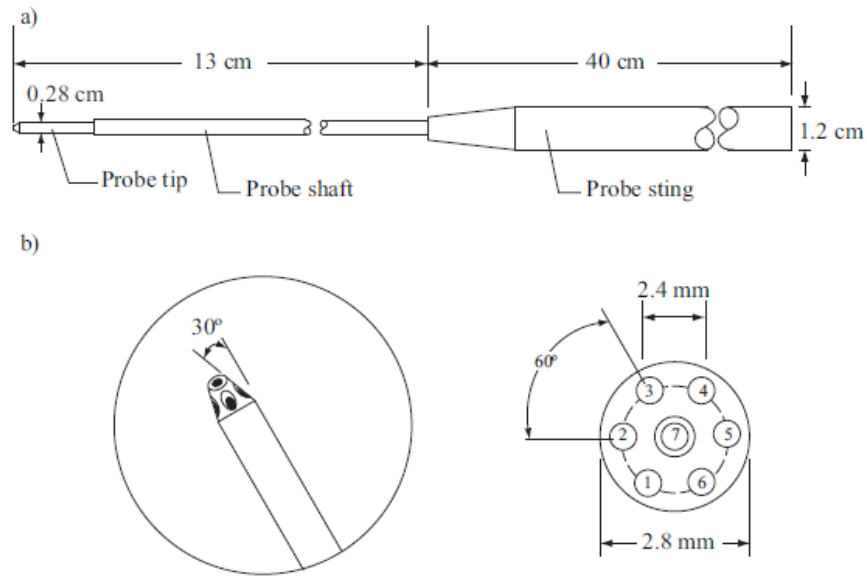
Figure 18 Schematic diagram for Seven-hole pressure probe
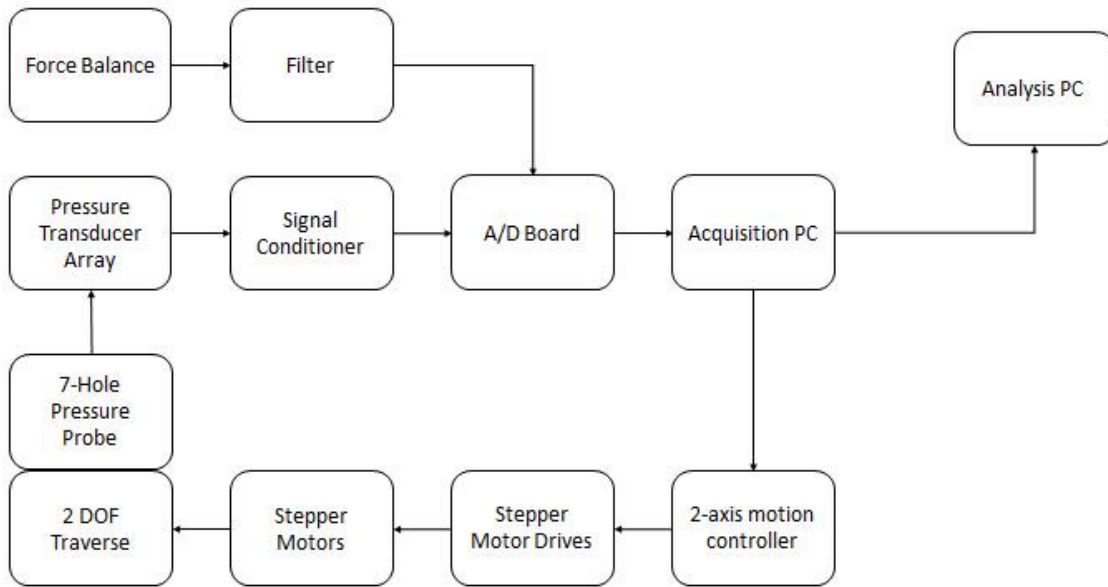
Figure 19 Data acquisition and reduction flow chart
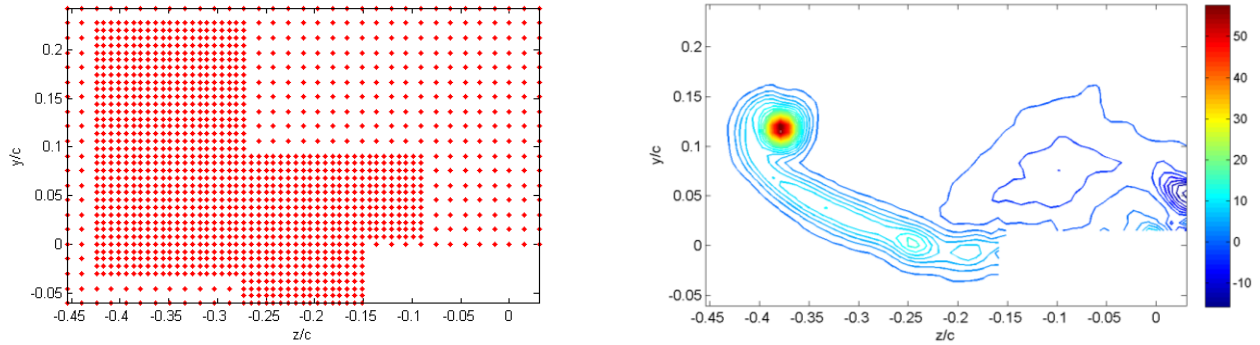
Figure 20 Scanning grid and sample iso-vorticity contour
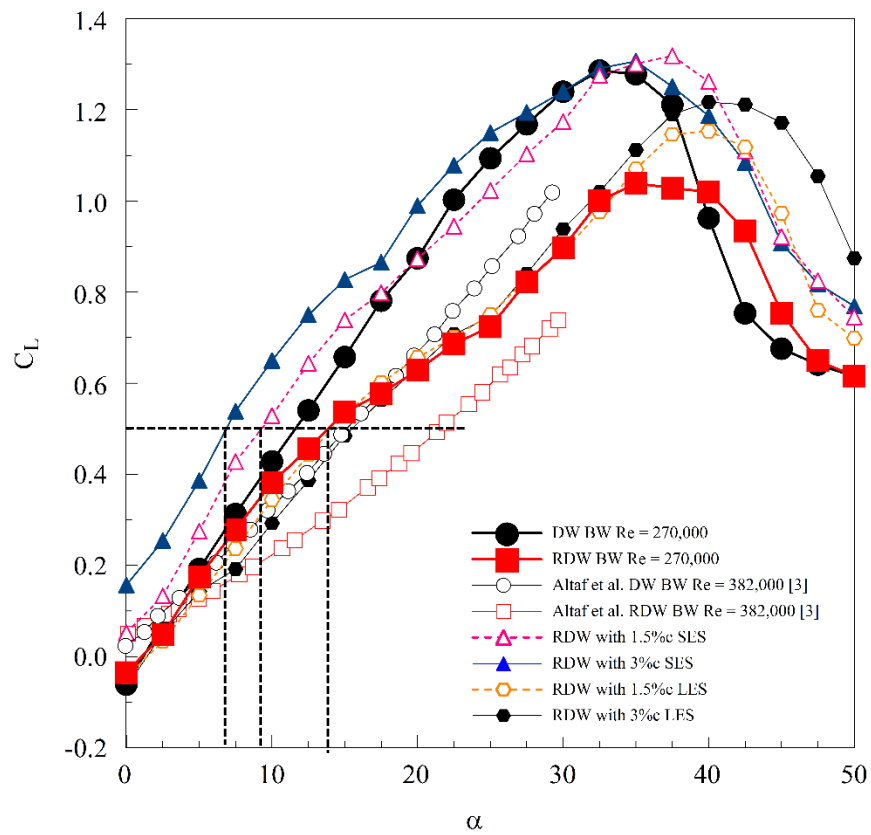
Figure 21 Lift coefficient verse **α** for different wing configurations
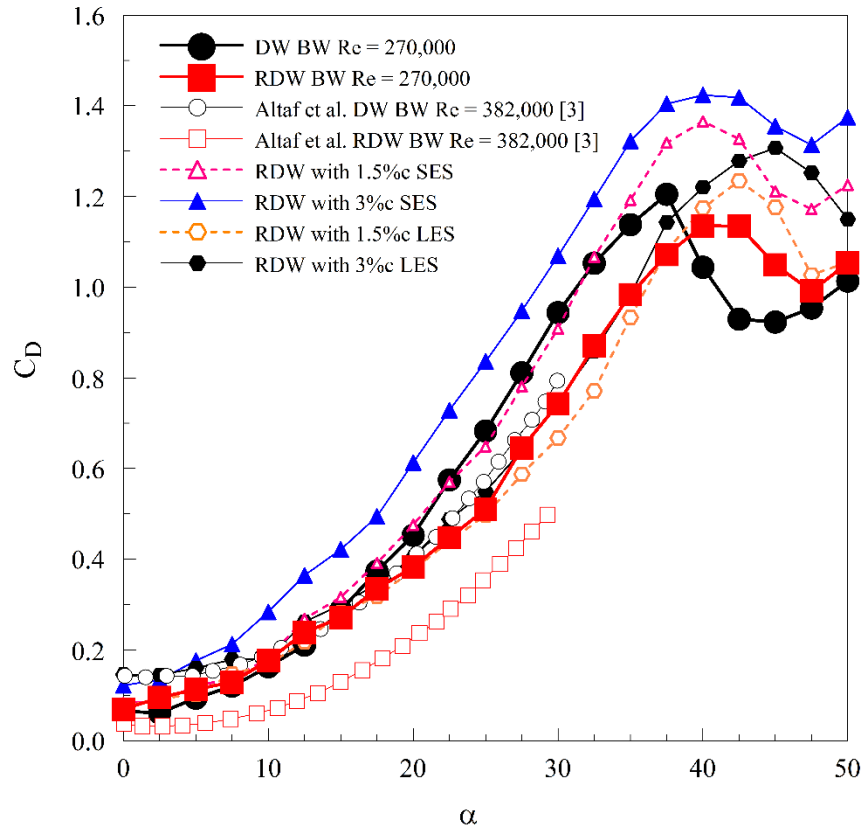
Figure 22 Drag coefficient verses angle of attack for different wing configurations
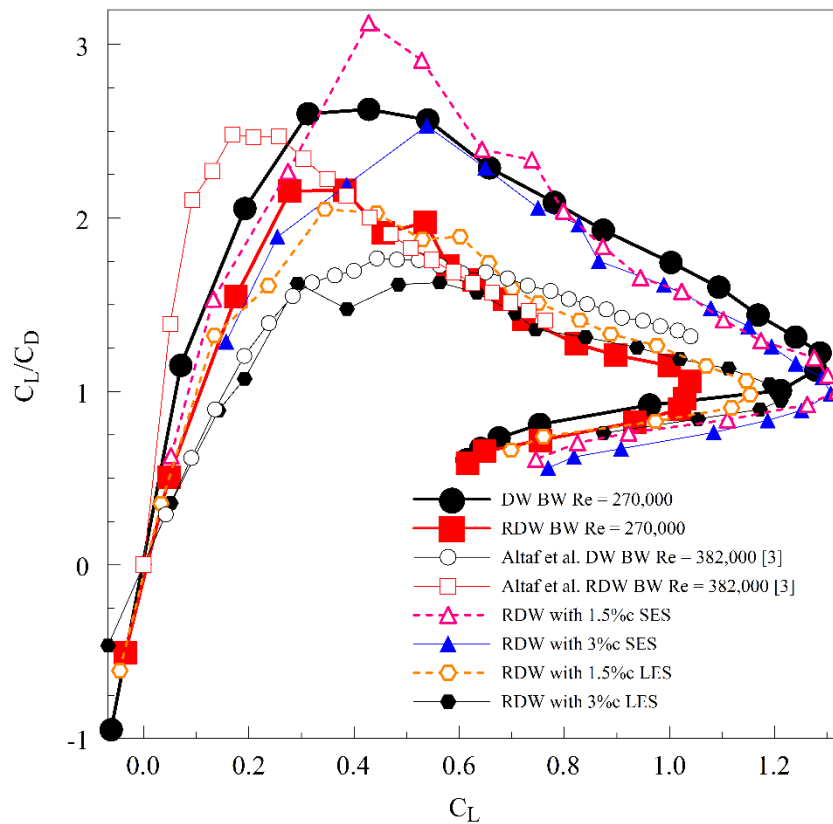
Figure 23 L/D verses lift coefficient for different wing configurations
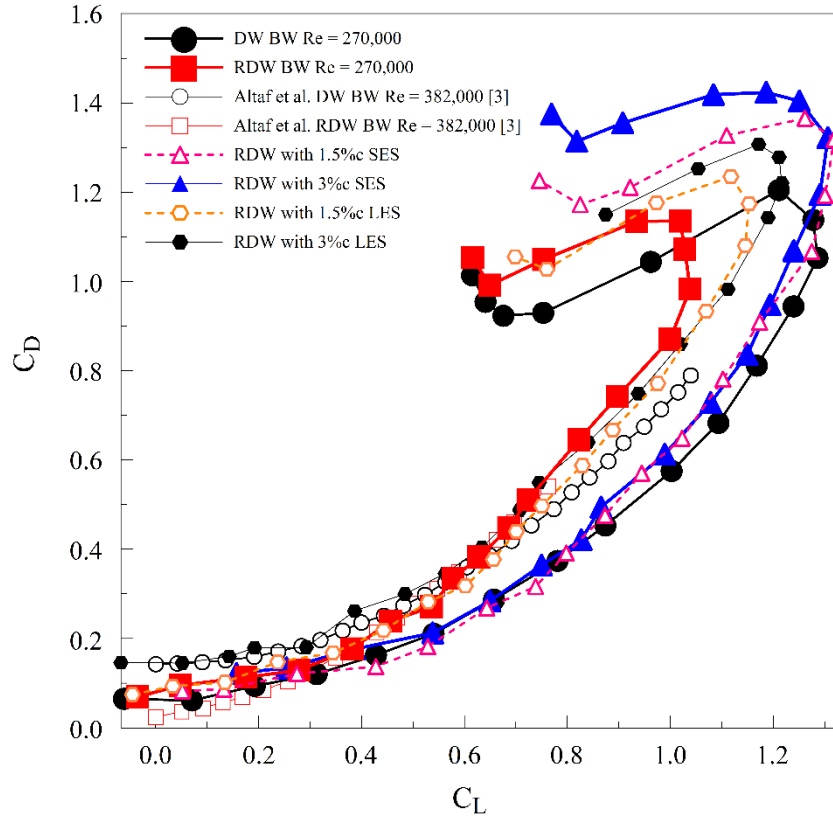
Figure 24 Drag polar diagram for different wing configurations
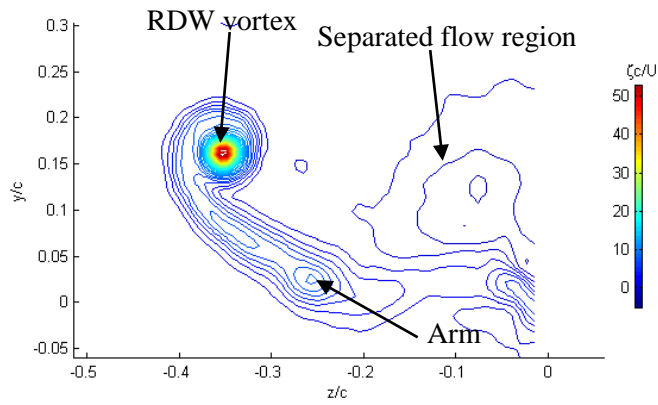
Figure 25 RDW tip vortices structure

70
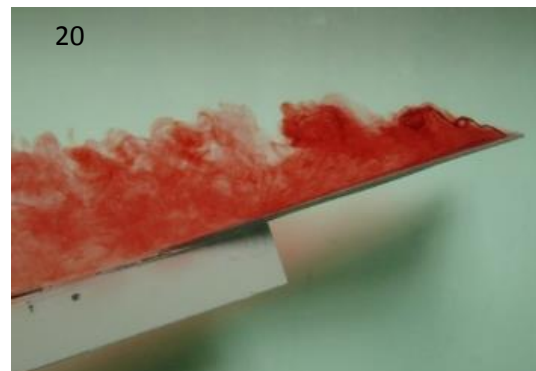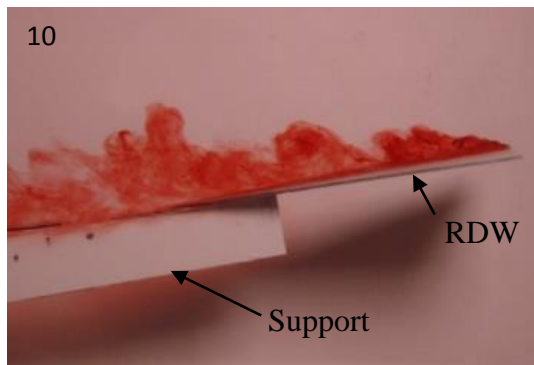
Figure 26 Dye flow visualization (middle injection) of RDW at $\alpha = 10^\text{o} - 40^\text{o}$

a)

Composite iso-vorticity contour plot for Delata Wing at $\alpha = 18^{\circ}$ Re = 270,000.
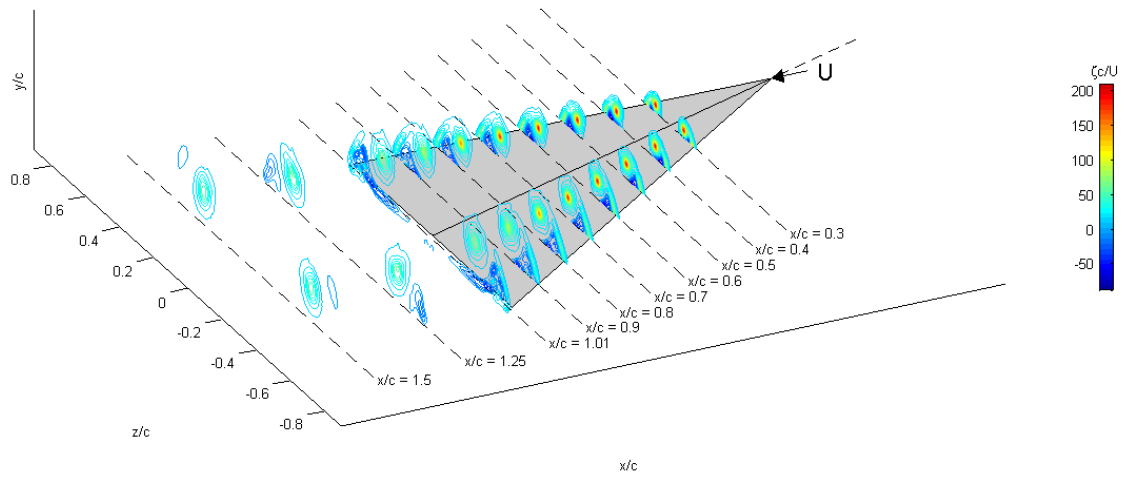
b)

Composite iso-vorticity contour plot for Reverse Delata Wing at $\alpha = 18^{\circ}$ Re = 270,000.
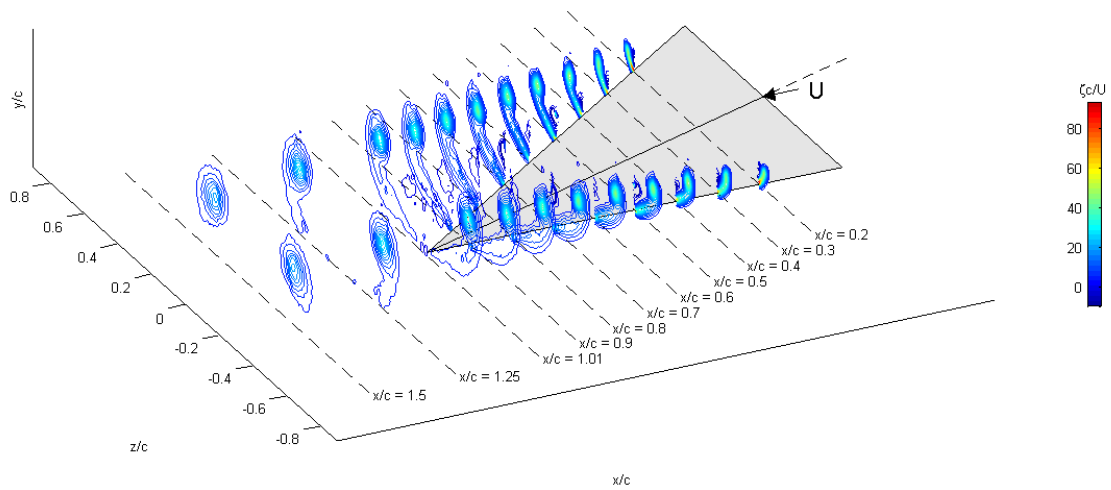

Figure 27 3-D iso-vorticity contour plot for a) Delta wing b) Reverse delta wing at $\alpha = 18^{\circ}$
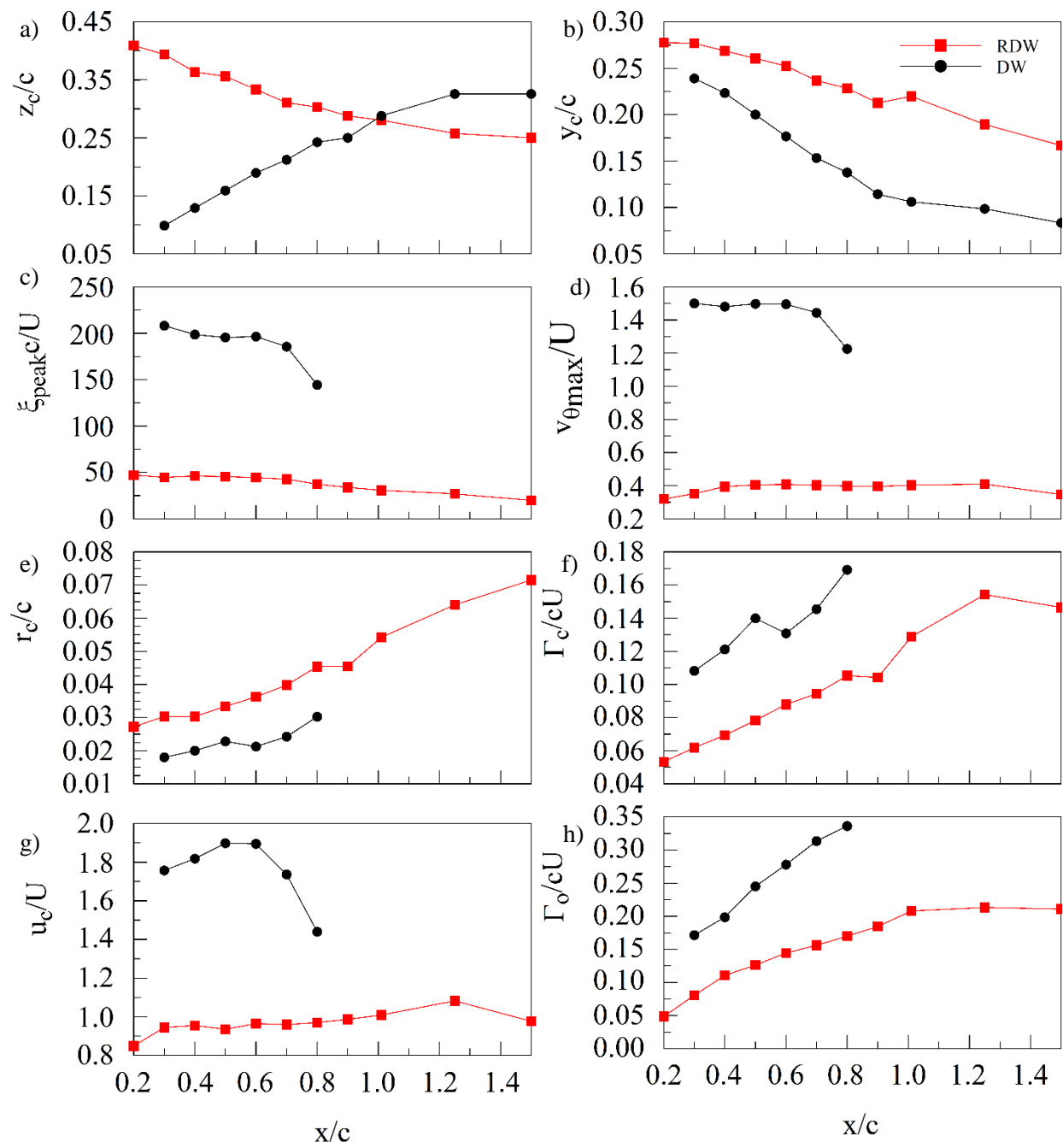
Figure 28 Important vortical flow quantities for DW and RDW at α = 18º

Composite iso-vorticity contour plot for Reverse Delata Wing at $\alpha = 10^{\circ}$ Re = 270,000.
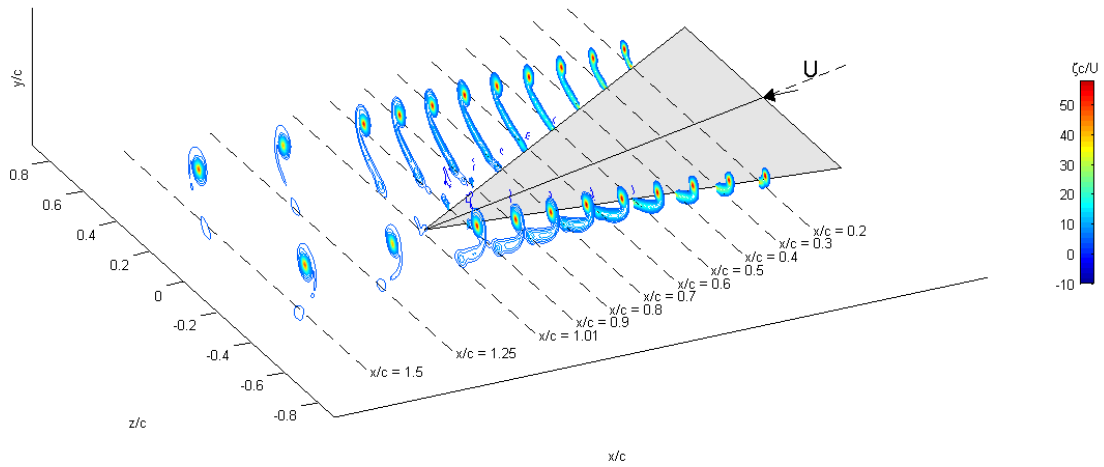
Figure 29 3-D iso-vorticity contour plot for RDW at $\alpha = 10^{\circ}$

Composite iso-vorticity contour plot for Reverse Delata Wing at $\alpha = 14^{\circ}$ Re = 270,000.
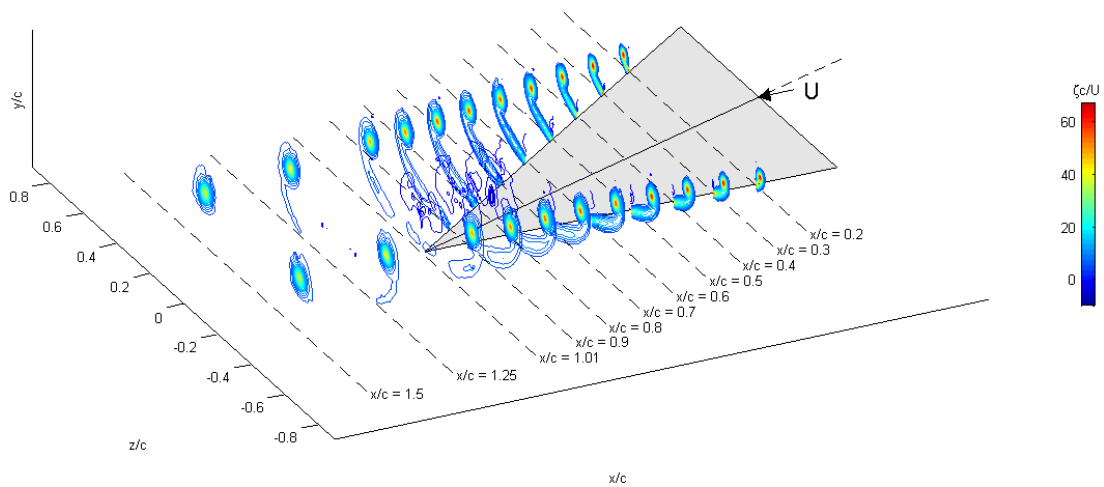
Figure 30 3-D iso-vorticity contour plot for RDW at $\alpha = 14^{\circ}$

Composite iso-vorticity contour plot for Reverse Delata Wing at $\alpha = 16^{\circ}$ Re = 270,000.
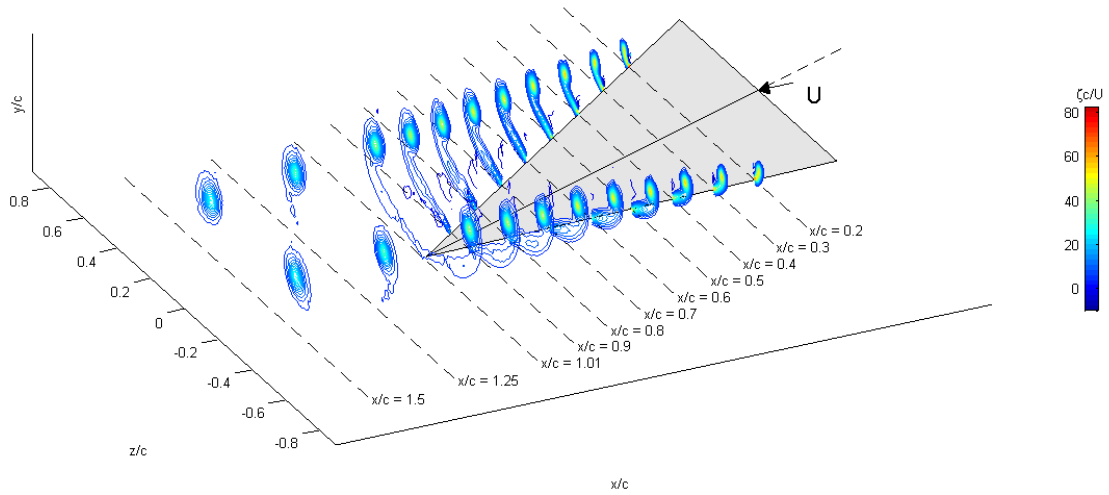
Figure 31 3-D iso-vorticity contour plot for RDW at α = 16º

Composite iso-vorticity contour plot for Reverse Delata Wing at $\alpha = 16^{\circ}$ Re = 270,000.
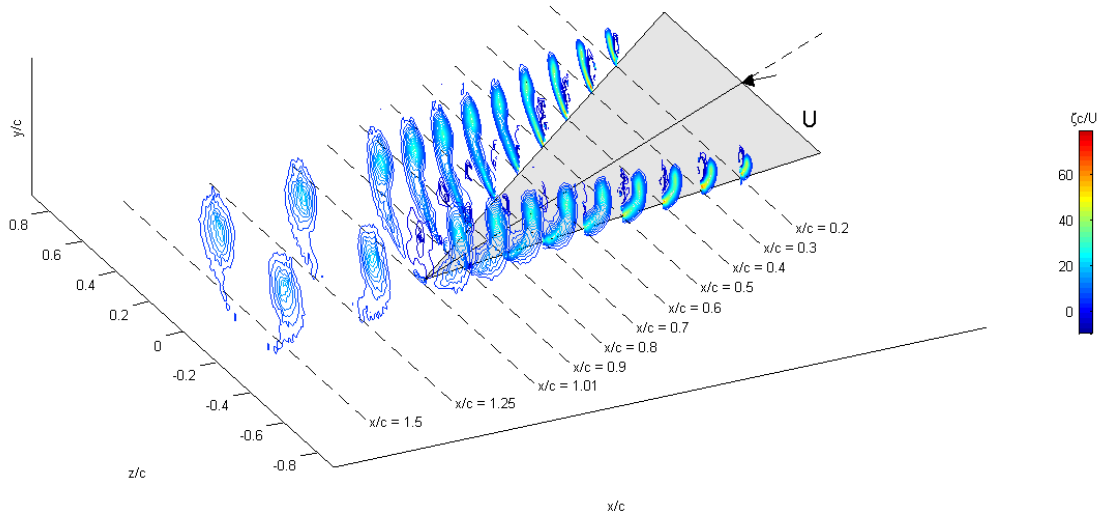
Figure 32 3-D iso-vorticity contour plot for RDW at α = 22º

75
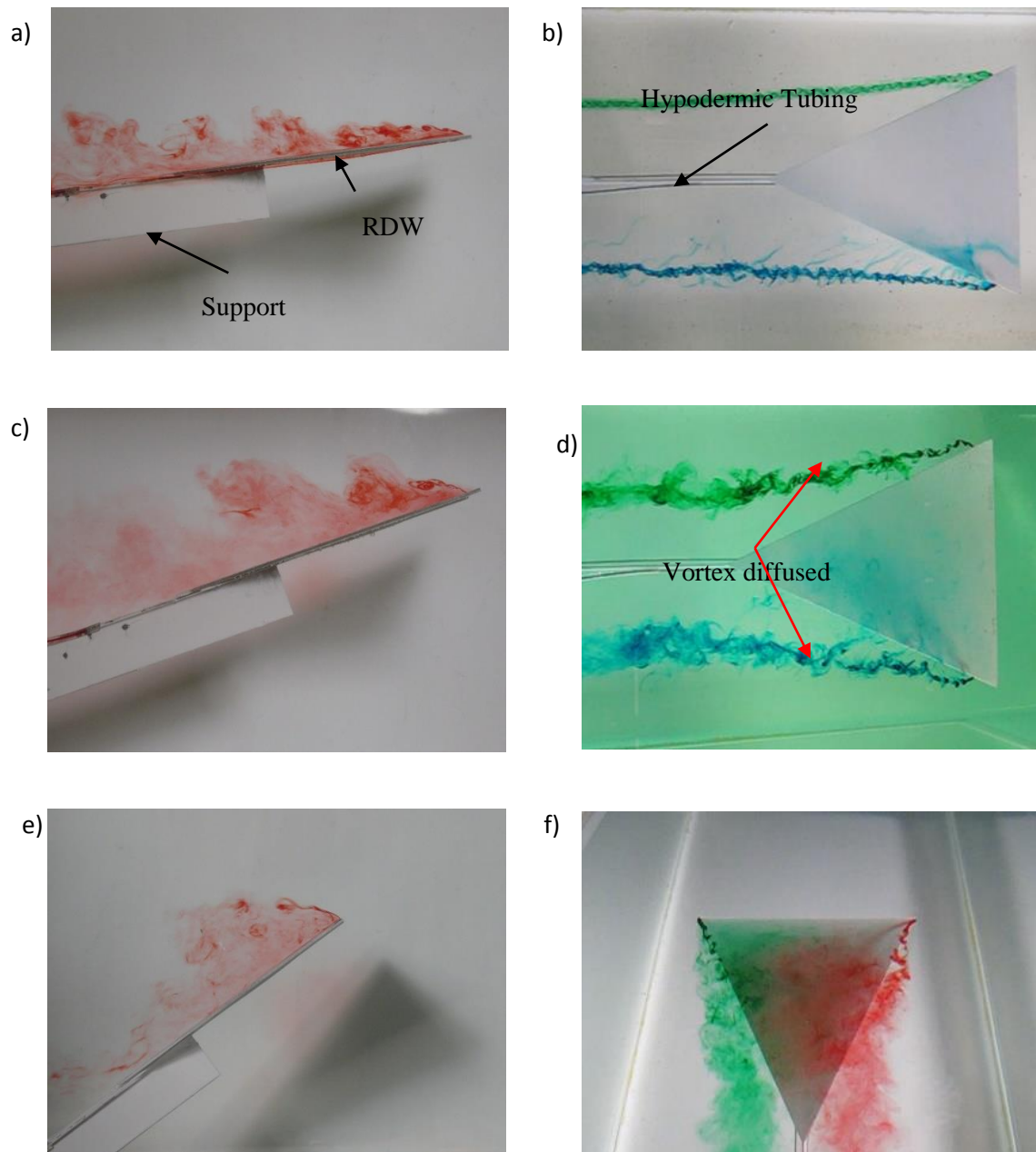
Figure 33 Dye flow visualization at $\alpha = 10^o, 20^o, 35^o$ a, c, e) middle injection side view b, d, f) side injection top view
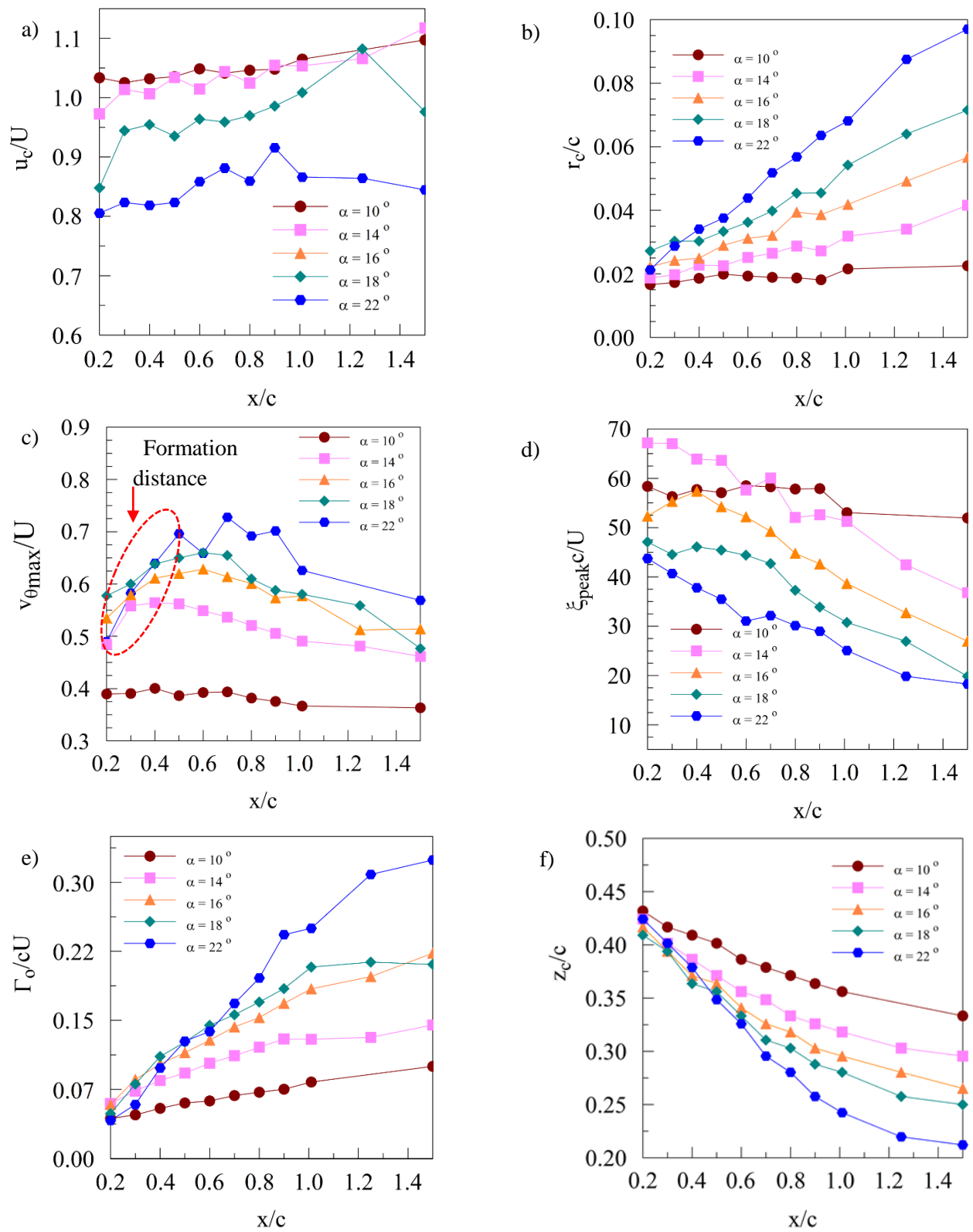
Figure 34 a) axial core velocity, b) core radius, c) maximum tangential velocity, d) peak vorticity, e) total circulation value, and f) vortex core locations verses spanwise direction
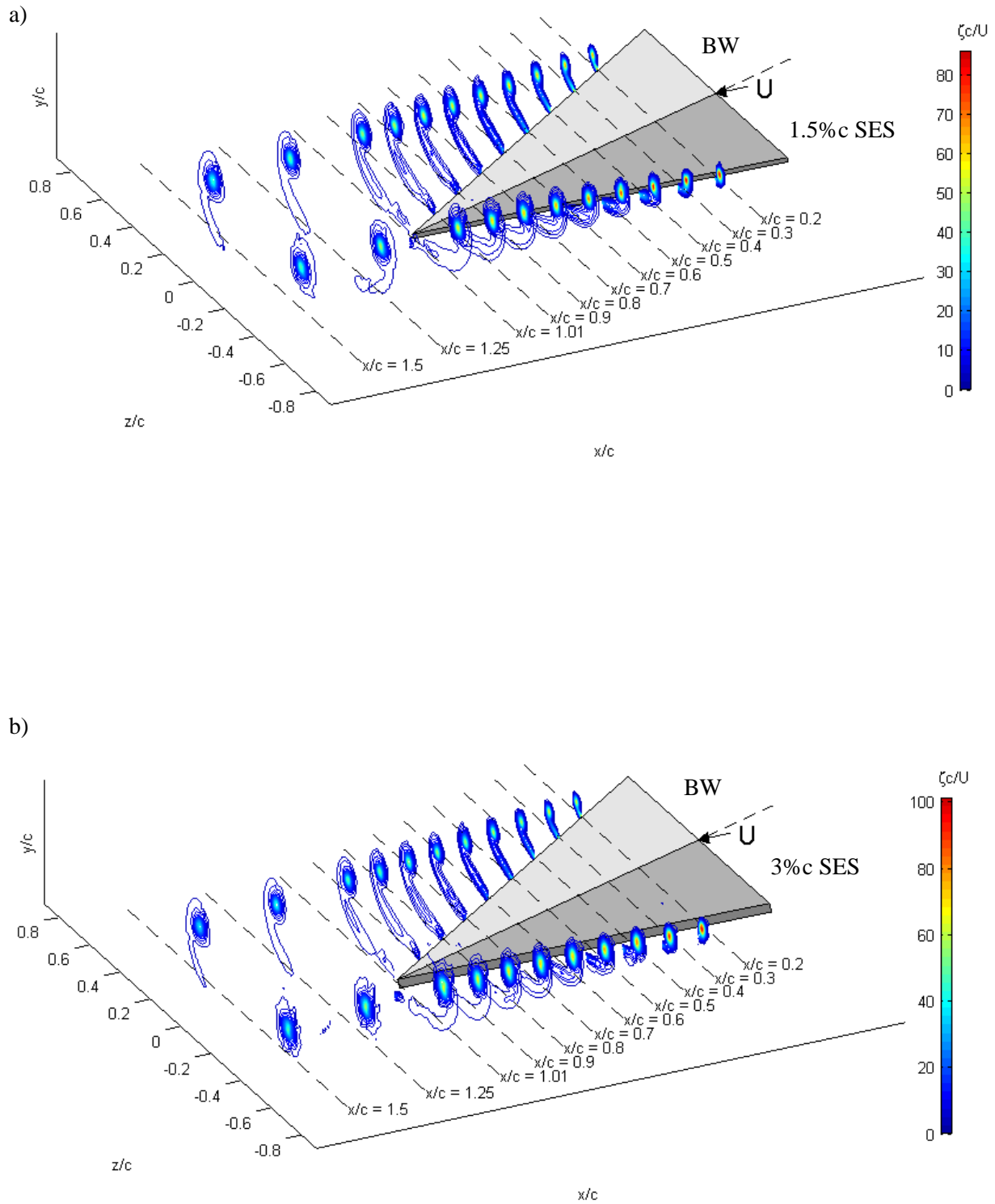
Figure 35 3-D iso-vorticity contour plot for a) wing with 1.5% c SES b) wing with 3% c SES at α = 14°
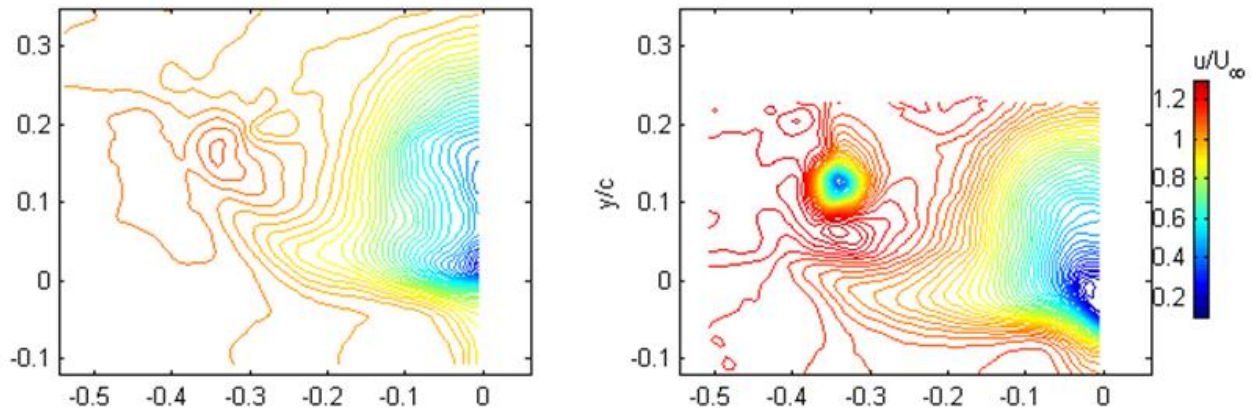
Figure 36 Iso-axial velocity contours for a) BW RDW, and b) 3% c SES
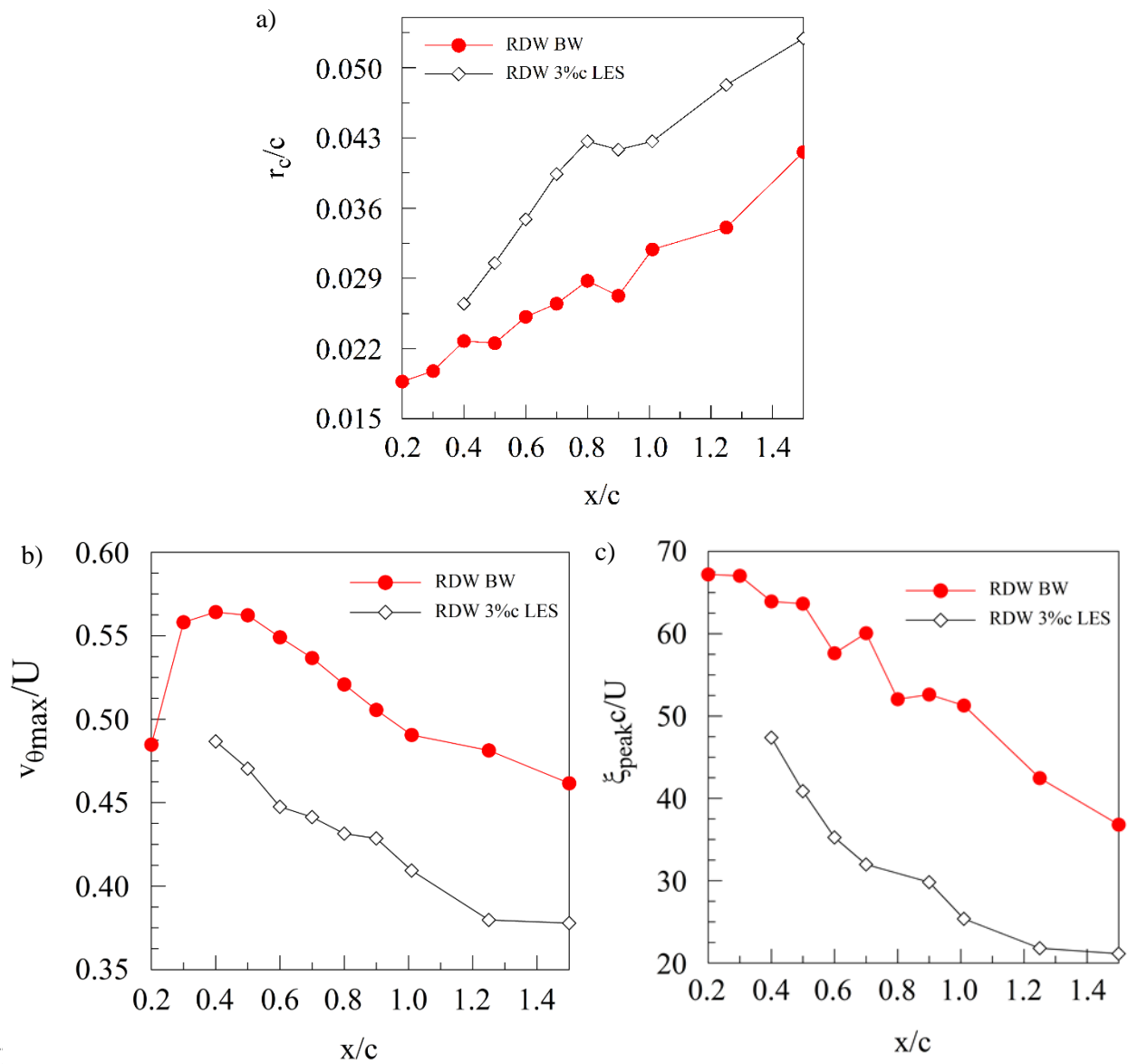
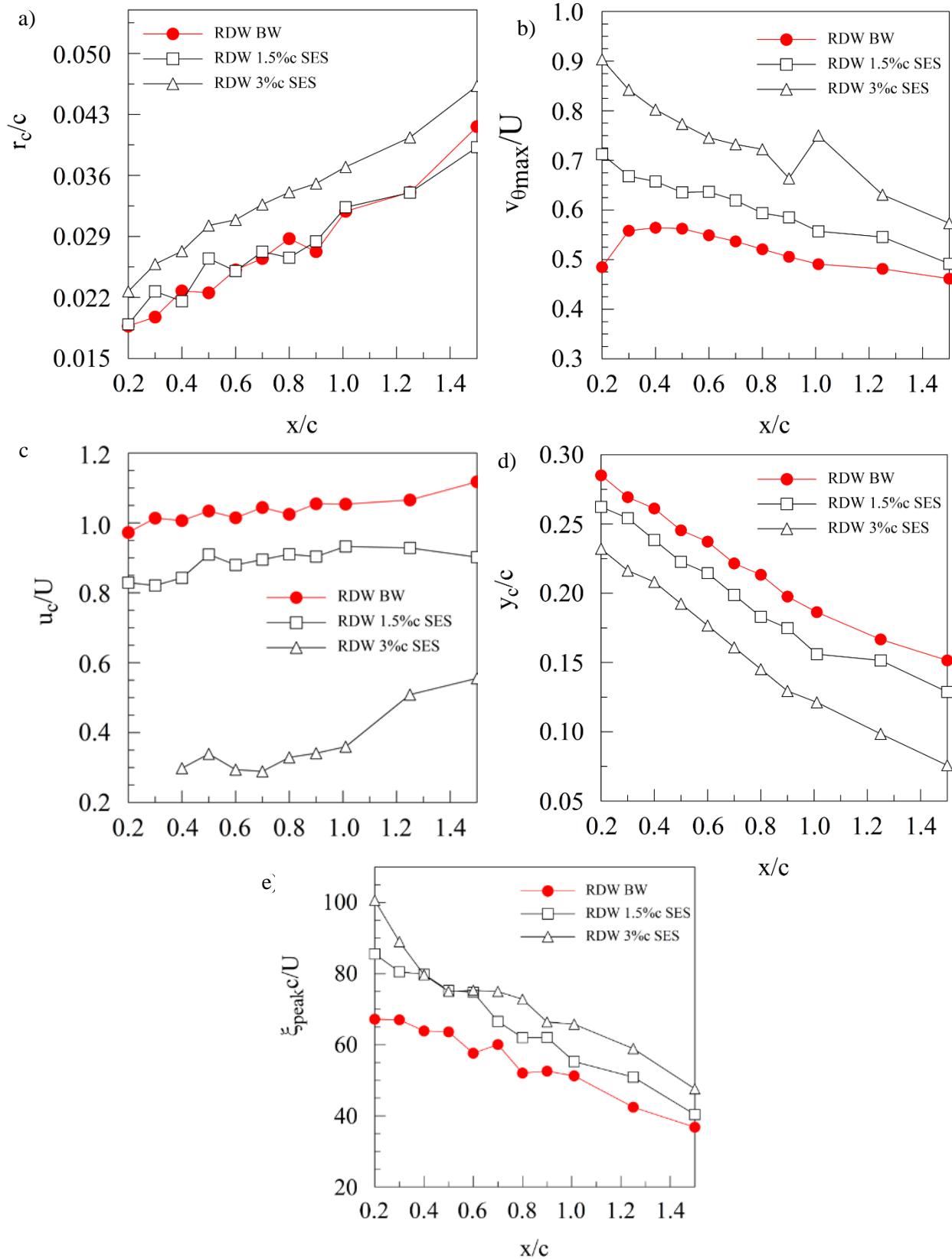Figure 37 a) Core radius, b) maximum tangential velocity, and c) peak vorticity vs. streamwise locations

Figure 38 a) Vortex core radius, b) maximum tangential velocity, c) core axial velocity, d) vertical core locations, and e) peak vorticity values verses streamwise locations at $\alpha = 24^{\circ}$
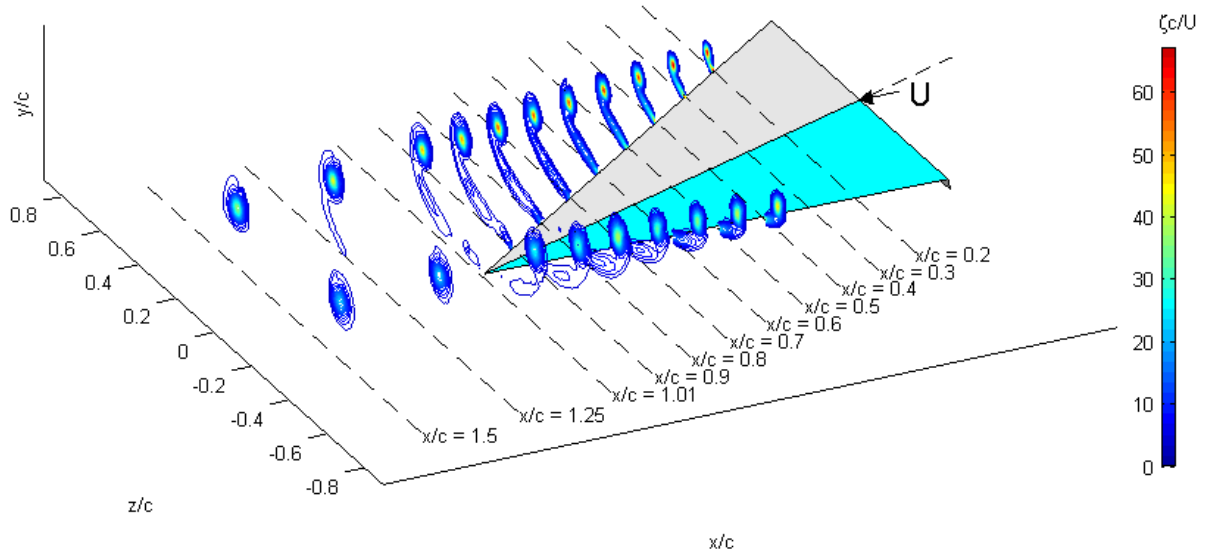
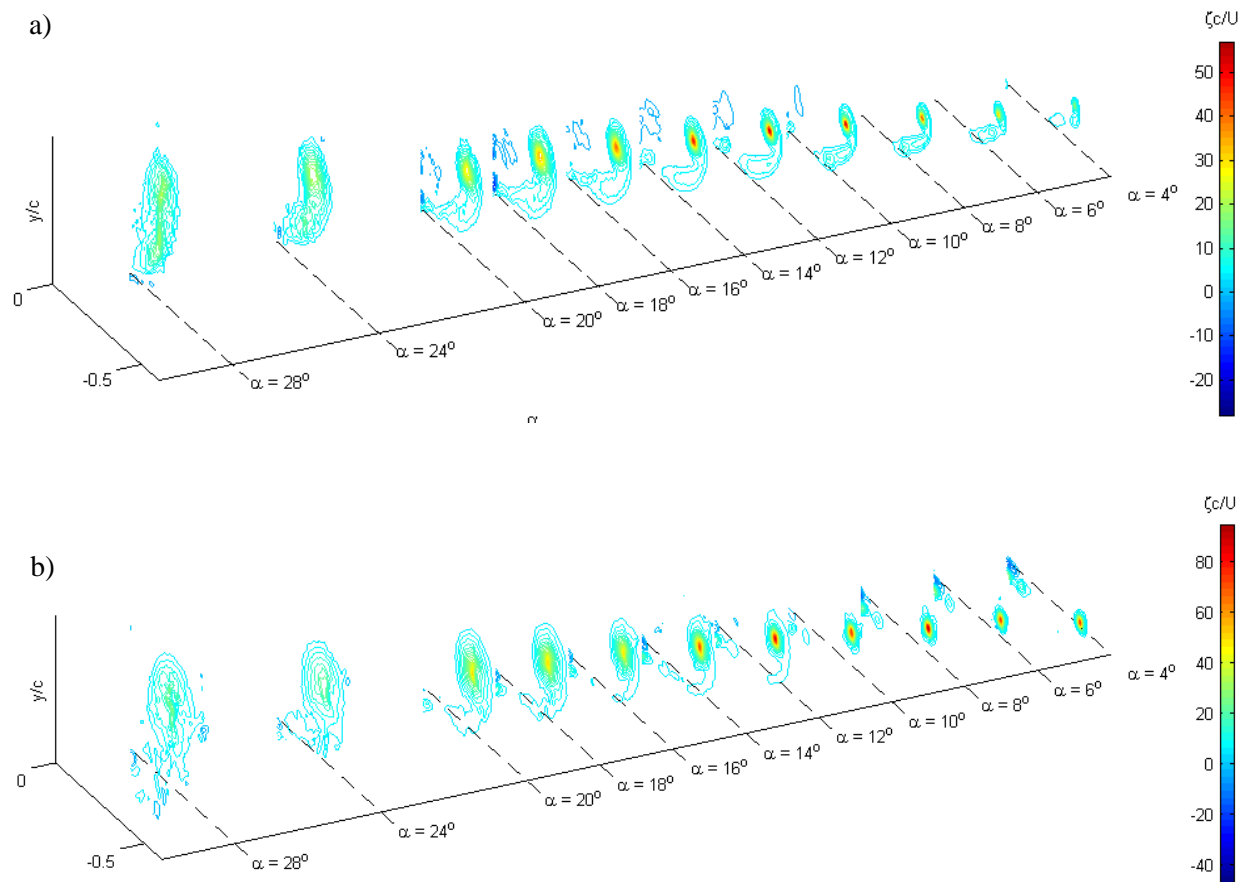Figure 39 Iso-vorticity contour of 3%c LES in direct comparison of a BW

Figure 40 Iso-vorticity contour of baseline RDW and wing with 3%c SES for $\alpha = 4^{\circ} - 28^{\circ}$
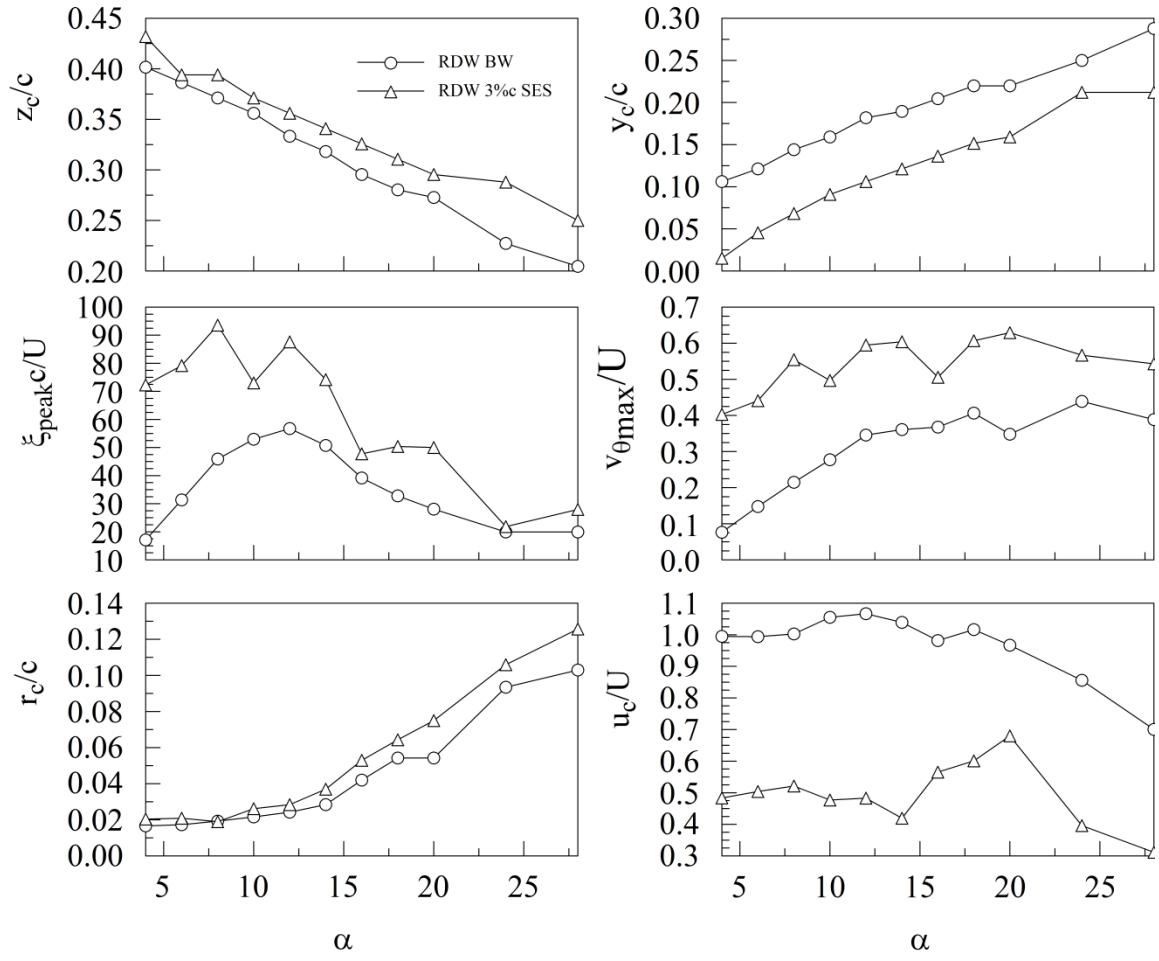
Figure 41 Important flow characteristics at a fixed location $\alpha = 4^o - 28^o$